

การประยุกต์ใช้งานเส้นลวดนาโนซิงค์ออกไซด์ที่สังเคราะห์ด้วยเทคนิค
ไฮโดรเทอร์มัลในอุปกรณ์กำเนิดพลังงานและอุปกรณ์เซนเซอร์ที่ยืดหยุ่นได้

APPLICATION OF HYDROTHERMAL ZINC OXIDE NANOWIRES IN
FLEXIBLE NANOGENERATOR AND SENSOR DEVICES

ชัยณัฐ จิรายุพัฒน์
CHAIYANUT JIRAYUPAT

วิทยานิพนธ์นี้เป็นส่วนหนึ่งของการศึกษาตามหลักสูตรปริญญาวิทยาศาสตรมหาบัณฑิต
สาขาวิชานาโนวิทยาและนาโนเทคโนโลยี
วิทยาลัยนาโนเทคโนโลยีพระจอมเกล้าลาดกระบัง
สถาบันเทคโนโลยีพระจอมเกล้าเจ้าคุณทหารลาดกระบัง

พ.ศ. 2560

KMITL-2018-NT-M-001-001

การประยุกต์ใช้งานเส้นลวดนาโนซิงค์ออกไซด์ที่สังเคราะห์ด้วยเทคนิค
ไฮโดรเทอร์มัลในอุปกรณ์กำเนิดพลังงานและอุปกรณ์เซนเซอร์ที่ยืดหยุ่นได้

APPLICATION OF HYDROTHERMAL ZINC OXIDE NANOWIRES IN
FLEXIBLE NANOGENERATOR AND SENSOR DEVICES

ชัยณัฐ จิรายุพัฒน์

CHAIYANUT JIRAYUPAT

วิทยานิพนธ์นี้เป็นส่วนหนึ่งของการศึกษาตามหลักสูตรปริญญาวิทยาศาสตรมหาบัณฑิต

สาขาวิชานาโนวิทยาและนาโนเทคโนโลยี

วิทยาลัยนาโนเทคโนโลยีพระจอมเกล้าลาดกระบัง

สถาบันเทคโนโลยีพระจอมเกล้าเจ้าคุณทหารลาดกระบัง

พ.ศ. 2560

KMITL-2018-NT-M-001-001

COPYRIGHT 2017

COLLEGE OF NANOTECHNOLOGY

KING MONGKUT'S INSTITUTE OF TECHNOLOGY LADKRABANG

หัวข้อวิทยานิพนธ์	การประยุกต์ใช้งานเส้นลวดนาโนซิงค์ออกไซด์ที่สังเคราะห์ด้วยเทคนิคไฮโดรเทอร์มัลในอุปกรณ์กำเนิดพลังงานและอุปกรณ์เซนเซอร์ที่ยืดหยุ่นได้
นักศึกษา	นายชัยณัฐ จิรายุพัฒน์
รหัสประจำตัว	58607012
ปริญญา	วิทยาศาสตรมหาบัณฑิต
สาขาวิชา	นาโนวิทยาและนาโนเทคโนโลยี
พ.ศ.	2560
อาจารย์ที่ปรึกษาวิทยานิพนธ์	ผู้ช่วยศาสตราจารย์ ดร.วินัดดา วงศ์วิริยะพันธ์
อาจารย์ที่ปรึกษาวิทยานิพนธ์ร่วม	ดร.อรรณพ คล้าชื่น

บทคัดย่อ

งานวิจัยนี้ศึกษาเกี่ยวกับศึกษาการสังเคราะห์ลวดนาโนซิงค์ออกไซด์ด้วยเทคนิคไฮโดรเทอร์มัลและการประยุกต์ใช้งานในอุปกรณ์นาโนที่ยืดหยุ่นได้ การดำเนินการวิจัยประกอบด้วยสี่ส่วนหลัก ได้แก่ ส่วนที่ 1 การศึกษาการสังเคราะห์ลวดนาโนซิงค์ออกไซด์ประกอบด้วย 2 ขั้นตอน ขั้นตอนที่ 1 คือ การศึกษาการสังเคราะห์ฟิล์มบางผลึกตั้งต้น ด้วยวิธีการเคลือบแบบหมุนเหวี่ยง และนำไปเผาที่อุณหภูมิ 100 - 600 องศาเซลเซียส พบว่าลักษณะของฟิล์มบางผลึกตั้งต้นที่เหมาะสมแก่การสังเคราะห์ลวดนาโนซิงค์ออกไซด์นอกจากจะมีความเป็นผลึกในระนาบ (002) ที่ดีแล้วยังต้องมีสัณฐานวิทยาที่สม่ำเสมอด้วย ขั้นตอนที่ 2 คือการศึกษาการสังเคราะห์ลวดนาโนซิงค์ออกไซด์ด้วยวิธีการไฮโดรเทอร์มอลโดยใช้สารตั้งต้นคือ ซิงก์ไนเตรทเฮกซะไฮเดรตกับเฮกซะเมทิลีนเตตระมีนในอัตราส่วน 1:1 ความเข้มข้น 5-100 มิลลิโมลาร์ เพื่อศึกษาการควบคุมขนาดและความหนาแน่นของลวดนาโนซิงค์ออกไซด์ พบว่าความเข้มข้นที่เพิ่มขึ้นส่งผลให้ขนาดของลวดนาโนซิงค์ออกไซด์เพิ่มขึ้นเนื่องจากอัตราการโตในระนาบ (100) สูงขึ้นจนส่งผลให้ลวดนาโนซิงค์ออกไซด์ผลสลายตัวกลายเป็นฟิล์มบางโดยสังเกตจากความหนาแน่นของลวดนาโนซิงค์ออกไซด์ที่ลดลงและมีสัดส่วนพื้นที่หน้าตัดของลวดนาโนซิงค์ออกไซด์ต่อพื้นที่ฐานรองรับที่สูงขึ้น ส่วนที่ 2 การศึกษาการเจือลวดนาโนซิงค์ ออกไซด์โดยโลหะเงินด้วยกระบวนการไฮโดรเทอร์มอลโดยใช้สารตั้งต้นของสารเจือคือซิลเวอร์ไนเตรท ที่ความเข้มข้นตั้งแต่ 0.2 - 1 มิลลิโมลาร์ พบว่าเมื่อปริมาณความเข้มข้นของโลหะเงินต่ำสามารถเจือโลหะเงินเข้าไปในผลึกลวดนาโนซิงค์ออกไซด์ได้โดยสัณฐานวิทยาของลวดนาโนซิงค์ออกไซด์ไม่มีการเปลี่ยนแปลงแต่เมื่อปริมาณความเข้มข้นของโลหะเงินสูงขึ้นพบว่าการโตของลวดนาโนซิงค์ออกไซด์ถูกขัดขวางจากการตกตะกอนร่วมของโลหะเงิน โดยปริมาณความเข้มข้นของโลหะเงินสูงสุดที่สามารถเจือเข้าไปในผลึกลวดนาโนซิงค์ออกไซด์ได้โดยไม่มี การ

เปลี่ยนแปลงของสัญญาณวิทยาคือ 0.36 เปอร์เซ็นต์โดยจำนวนอะตอม ส่วนที่ 3 การประยุกต์ใช้ลวดนาโนซิงค์ออกไซด์กับอุปกรณ์นาโนอิเล็กทรอนิกส์ โดยส่วนนี้จะแบ่งออกเป็นสองส่วนย่อย ส่วนย่อยแรกสาธิตการนำไปพัฒนาประสิทธิภาพอุปกรณ์กำเนิดพลังงานไฟฟ้าจากแรงเสียดทานโดยการเพิ่มความหนาแน่นประจุไฟฟ้าเหนี่ยวนำด้วยวัสดุเพียโซอิเล็กทริกลวดนาโนซิงค์ออกไซด์ หรือ พีไอทีโดยใช้วัสดุเพียโซอิเล็กทริกลวดนาโนซิงค์ออกไซด์เพื่อเพิ่มประสิทธิภาพการส่งถ่ายประจุจากอะลูมิเนียมสฟัลไฟด์เมทิลซิลิโคนโดยอุปกรณ์ พีไอทีสามารถให้กำลังไฟฟ้าสูงสุดได้ถึง 0.5 มิลลิวัตต์ต่อตารางเซนติเมตร ภายใต้แรงขนาด 8.5 นิวตัน สูงกว่าอุปกรณ์กำเนิดพลังงานไฟฟ้าจากแรงเสียดทานแบบปกติถึง 100 เท่า และส่วนย่อยสองคือการสาธิตเป็นอุปกรณ์ก๊าซเซนเซอร์แบบยืดหยุ่นได้ที่ประดิษฐ์จากลวดนาโนซิงค์ออกไซด์ที่สังเคราะห์บนลวดนาโนซิงค์ออกไซด์ที่ฝังตัวในพอลิไดเมทิลซิลิโคน โดยทดสอบประสิทธิภาพการตอบสนองภายใต้สภาพปกติและภายใต้การโค้งงอที่ 30 และ -30 องศา พบว่าสามารถตอบสนองไอระเหยของเอทานอลได้เสถียรแม้จะอยู่ภายใต้สภาพการโค้งงอ

คำสำคัญ : ลวดนาโนซิงค์ออกไซด์, ลวดนาโนซิงค์ออกไซด์เจืออนุภาคเงิน, อุปกรณ์นาโนยืดหยุ่นได้, อุปกรณ์กำเนิดพลังงานไฟฟ้าจากแรงเสียดทาน, เพียโซอิเล็กทริก, ก๊าซเซนเซอร์

Thesis Title	APPLICATION OF HYDROTHERMAL ZINC OXIDE NANOWIRES IN FLEXIBLE NANOGENERATOR AND SENSOR DEVICES
Student	Mr. Chaiyanut Jirayupat
Student ID	58607012
Degree	Master of Science
Program	Nanoscience and Nanotechnology
Year	2017
Thesis advisor	Asst. Prof. Dr. Winadda Wongwiriyan
Thesis Co-advisor	Dr. Annop Klamchuen

ABSTRACT

This research has focused on fundamental study of hydrothermal zinc oxide nanowires (ZnO NWs) and their applications for flexible nano-devices. This research consists of 3 parts. The first part has studied on synthesis of ZnO NWs, which including 2 processes. The first process is preparation of ZnO seed layer by spin coating and heat treatment at 100 to 600 degree Celsius. It was found that the properties of ZnO seed layer required for hydrothermal ZnO NWs are not only high crystallinity in (002) plane but also high uniformity of particle size. The second process is synthesis of ZnO NWs via hydrothermal process by using zinc nitrate hexahydrate and hexamethylenetetramine as an initial chemical precursor in an equal molar concentration in a range of 5 to 100 mM for control of size and density of ZnO NWs. When the concentration increases, the size of the ZnO NWs increases due to a high growth rate in the ZnO (100) plane and finally ZnO NWs were merged into thin films. This can be observed from a decrease in ZnO NWs density and an increase in an area faction. The second part of the research has studied on the synthesis of Ag-doped ZnO NWs. The growth precursors with different Ag concentrations were prepared by mixing different concentrations of silver nitrate in a range of 0.2 to 1 mM into the initial ZnO precursor. When the Ag concentration was relatively low, the Ag-doped ZnO NWs shows a preferred growth orientation of (002) direction with no obvious change of morphology. In contrast, for a relatively high Ag

concentration, the ZnO NWs growth was suppressed by Ag ion due to self-precipitation of Ag. The maximum Ag concentration in the Ag-doped ZnO NWs was 0.36 at.% with a well-defined structure of the Ag-doped ZnO NWs. The third part of the research is application of ZnO NWs for flexible nano-devices, which including 2 sections. In the first section, a hybrid nanogenerator based on a novel device structure (ZnO NWs connected to the top Au electrode of Au/PDMS-Al triboelectric structure) was demonstrated to enhance an electrical output of triboelectric nanogenerator through piezoelectric effect as called piezo-induced triboelectric nanogenerator (PIT). By utilizing the piezo-potential of ZnO NWs for enhance the charge transfer from Al to PDMS, the maximum power density of PIT device is 0.5 mW/cm², which 100 times higher than general triboelectric device (Au/PDMS-Al) under an external applied force of 8.5 N. In the second section, a flexible gas sensor based on ZnO NWs grown on ZnO NWs-embedded PDMS (ZnO/ZnO/PDMS) was demonstrated. The gas sensor shows a stable response to ethanol vapor although the ZnO/ZnO/PDMS was bent upward and downward 30 degree.

Keywords : Zinc oxide nanowires, Ag-doped zinc oxide nanowires, Flexible nanodevices, Triboelectric nanogenerator, Piezoelectric, Gas sensor

ACKNOWLEDGEMENTS

I would first like to thank my thesis advisor Asst. Prof. Dr. Winadda Wongwiriyan (College of Nanotechnology, King Mongkut's Institute of Technology Ladkrabang (KMITL)) and co-advisor Dr. Annop Klamchuen (National Nanotechnology Center (NANOTEC)) for the continuous support of my research, for their patience, motivation and immense knowledge.

I would like to thank my thesis committees, Asst. Prof. Dr. Thutiyaporn Thiwawong, Dr. Sakon Rahong (College of Nanotechnology, KMITL) and Dr. Mati Horprathum (National Electronics and Computer Technology Center (NECTEC)) for their helpful advice, interest questions, insightful comments and suggestions in general.

I would like to acknowledge the financial support from the Thailand Graduate Institute of Science and Technology from National Science and Technology Development Agency (NSTDA).

Finally, I would like to thank all the colleagues and friends, especially the members of Nanocarbon Materials Research Laboratory (College of Nanotechnology, KMITL), Nano Characterization Laboratory and Integrated Nanosystem Laboratory (NANOTEC) for their supports.

Chaiyanut Jirayupat

CONTENTS

	Page
บทคัดย่อ.....	I
ABSTRACT.....	III
ACKNOWLEDGEMENTS.....	V
CONTENTS.....	VI
LIST OF TABLES.....	IX
LIST OF FIGURES.....	X
CHAPTER 1 INTRODUCTION	1
1.1 Significance of research.....	1
1.2 Objectives of the study	3
1.3 Scope of the study.....	3
1.4 Expected results	5
CHAPTER 2 LITERATURE REVIEW AND THEORETICAL BACKGROUND.....	6
2.1 Zinc oxide.....	6
2.2 Zinc oxide nanowire.....	7
2.2.1 Synthesis of zinc oxide nanowire.....	9
2.3 Zinc oxide seed layer.....	12
2.3.1 Sputtering technique	12
2.3.2 Sol-gel technique	14
2.4 Nanogenerators	15
2.4.1 Piezoelectric nanogenerator based on ZnO nanowire.....	15
2.4.2 Triboelectric nanogenerator.....	16
2.5 Gas sensors.....	18
2.5.1 Gas sensors based on ZnO nanowire.....	19

CONTENTS (Cont.)

	Page
CHAPTER 3 MORPHOLOGY CONTROL OF HYDROTHERMAL ZINC OXIDE NANOWIRES.....	20
3.1 Synthesis of ZnO nanowires by seed-assisted hydrothermal.....	20
3.1.1. Synthesis of ZnO seed layer.....	20
3.1.2 Synthesis of ZnO nanowires by ZnO seed layer	21
3.2 Effect of ZnO seed layer on morphology of ZnO nanowires	21
3.3 Effect of ZnO precursor concentration on morphology of ZnO nanowires .	26
CHAPTER 4 SYNTHESIS AND CHARACTERIZATION OF SILVER-DOPED ZINC OXIDE NANOWIRES BY HYDROTHERMAL	29
4.1 Synthesis of Ag-doped ZnO nanowires	29
4.2 Characterization of Ag doped ZnO nanowires.....	30
CHAPTER 5 APPLICATION OF ZINC OXIDE NANOWIRES FOR FLEXIBLE NANODEVICE	36
5.1 Synthesis of stretchable ZnO nanowires on ZnO nanowires-embedded polymer.....	36
5.2 Stretchable ZnO nanowires array for piezoelectric-induced triboelectric (PIT) device	37
5.2.1 Fabrication of Stretchable ZnO nanowires array for piezoelectric- induced triboelectric (PIT) device	37
5.2.2 Performance of hybrid nanogenerator device base on stretchable ZnO nanowires array	38
5.3 Stretchable ZnO nanowires array for hybrid nanogenerators Volatile organic compound (VOC) sensor.....	50
5.3.1 Fabrication of stretchable ZnO nanowires array for VOC sensor	50
5.3.2 Performance of VOC sensor based on stretchable ZnO nanowires array	52

CONTENTS (Cont.)

	Page
REFERENCES.....	54
AUTHOR BIBLIOGRAPHY	59

LIST OF TABLES

Table	Page
2.1. ZnO properties	7
3.1 Crystallinity and morphology of ZnO seed	24

LIST OF FIGURES

Figure	Page
1.1 The summary of the study scope.....	4
2.1 ZnO structure (a) The wurtzite structure model (b) the Zinc blende unit cell.	6
2.2 Nanostructures of ZnO.....	8
2.3 (a) The sensitivity and the repeatability of ZnO nanowires arrays based gas sensor. (b) Schematic gas sensing mechanism of ZnO nanowire in air and in presence of reducing gas (H ₂ or CO).....	8
2.4 (a) ZnO nanowire nanogenerators. (b) Short circuit current measurement of ZnO nanowire	9
2.5 (a) A schematic of the solar cells with ZnO nanowire heterojunctions, (b) A photograph of standard solar cells. (c) Cross-section SEM image of the ZnO nanowire solar cells	9
2.6 The schematic of VLS growth	10
2.7 The schematic of Seed-assisted hydrothermal techniques	12
2.8 Sputtering of atoms from a target surface under the influence of incident ions	13
2.9 Schematic view of the sputtering system.	13
2.10 Schematic of sol-gel process.....	15
2.11 (a) Piezoelectric model of wurtzite-structured ZnO. (b) Piezopotential of a stretched ZnO nanowire. (c) SEM image of ZnO nanowire.	17
2.12 Working principle of Vertical contact-separation mode of triboelectric nanogenerator..	17

2.13	Triboelectric Series for Materials Following a Tendency To Easily Lose Electrons (Positive) and to Gain Electrons (Negative).....	18
3.1	XRD spectrum of ZnO seed layer annealed with different temperature from 100°C to 600°C.	23
3.2	Figure 3.2 AFM images of ZnO seed layer annealing at (a) 400°C (b), 500°C (c) and 600°C	23
3.3	SEM images of ZnO NWs synthesized from ZnO seed layer annealing at (a) 400°C, (b) 500°C, and (c) 600°C,.....	24
3.4	Relationship between the size of ZnO NWs and the size of the ZnO seed layer compared to the annealing temperature of the ZnO seed layer.	25
3.5	The relationship between the density of ZnO NWs and density of ZnO seed layer particle compared to annealing temperature of ZnO seed layer	25
3.6	SEM image of ZnO NWs synthesized by hydrothermal with different concentration from 5 mM to 100 mM.....	27
3.7	The relationship between the size and density of ZnO NWs relative to the ZnO precursor concentrations of 5, 10, 20, 40 and 100 mM.....	28
3.8	Area fraction of different ZnO precursor concentration at 5, 10, 20, 40 and 100 mM.....	28
4.1	SEM image of ZnO NWs synthesized by hydrothermal with different concentration of AgNO ₃ from 0 mM to 1 mM	32
4.2	Relationship between size of ZnO NWs with different concentration of AgNO ₃ ranging from 0-1 mM	33
4.3	Relationship between length of ZnO NWs with different concentration	

of AgNO ₃ ranging from 0-1 mM.....	33
4.4 Relationship between density of ZnO NWs with different concentration of AgNO ₃ ranging from 0 to 1 mM.....	34
4.5 Relationship between Ag atomic concentrations of individual ZnO NWs from EDX in the TEM with different concentration of AgNO ₃ ranging from 0 to 0.6 mM.....	34
4.6 Ag 3d XPS spectrums of Ag doped ZnO NWs with different concentration of AgNO ₃ ranging from 0 to 1 mM.	35
5.1 SEM image of ZnO NWs grown on ZnO NW-embedded PDMS after 2 nd step growth.....	37
5.2 (a) Shows a schematic diagram of hybrid device (b) the total active area size of hybrid device is 1.5×1.5 cm ² (c) the cross-section image of ZnO NWs.....	38
5.3 (a) Show the cross-section of hybrid device and (d) RT device, which were applied by vertical force of 0.8 N on the topside (b) the open circuit voltage (Voc) and (c) short circuit current (Isc) of sub-device Z1, Z2 and Z3 as a function of time (e) the Voc and (f) Isc of sub-device T1, T2 and T3 at the different of time.....	41
5.4 (a) shows a schematic diagram of hybrid device (b) the total active area size of hybrid device is 1.5×1.5 cm ² (c) the cross-section image of ZnO NWs.....	41
5.5 Calculated variation of surface charge density (σ) and time (t) at different load resistances of R1=10 ¹¹ , R2=10 ¹³ , and R3=10 ¹⁵ Ω	44
5.6 Force profile in a single press-and-release as a function of time.....	45
5.7 (a) The cross-section of hybrid device without Al (b) the Voc and (c) Isc value of sub-device Z3 applied by external force from topside.....	45

5.8 (a) Demonstrate the Voc and (b) Isc value of sub-device Z3 applied by external force from topside (red line) and bottom side (blue line) at various force frequency.....	47
5.9 (a) The cross-section of hybrid device with Ag doped ZnO NWs (b) the Voc and (c) Isc value of sub-device Z3 applied by external force from topside	47
5.10 (a) The output voltage and (b) current at various resistances of sub-device Z3 and conventional triboelectric sub-device T3 (c) the peak power densities corresponding to load resistances are calculated as the product of corresponding current and voltage of sub-device Z3 and (d) triboelectric sub-device T3.....	48
5.11 Show (a) 100 LEDs in the series connected (b) the output power from device Z3 without any external load resistor could light up to 100 LEDs (c) the Voc and (d) current density output value during applied finger force.....	49
5.12 Schematic view of Stretchable gas sensor device	50
5.13. The resistivity-time curves of ZnO NWs when UV light is on and off.	52
5.14 Selectivity measurements of ZnO NWs for Ethanol, Acetone and Methanol.....	52
5.15 Ethanol sensing response of stretchable gas sensor while bending with different angles from -30° to 30°	53

CHAPTER 1

INTRODUCTION

1.1 Significance of Research

Zinc oxide nanowire (ZnO NW) has been widely studied due to their unique properties such as a non-centrosymmetric crystal structure, a wide direct band gap of ~ 3.37 eV at room temperature and a high exciton binding energy of 60 meV at room temperature. Recently, ZnO NW has been demonstrated as a candidate for a wide range of applications such as light-emitting diode, UV emitter and detector, solar cell, nanogenerator and gas sensor¹⁻⁶.

Since the morphology of ZnO NW directly corresponds to their properties, to maximize the performance of the ZnO NW-based integrated devices, most efforts have been focused on the morphology control of ZnO NW, especially the crystallinity, diameter, length, density and doping of ZnO NW⁷⁻¹⁰. Among fabrication methods, hydrothermal process is widely used for the synthesis of ZnO NW because of its low cost, catalyst free, and compatibility with various substrates including organic substrates for flexible and wearable electronic applications¹¹⁻¹³. Regarding the crystallinity of hydrothermal-grown ZnO NW, the most essential key is a control of preferential nucleation at the ZnO (0001) polar plane and a suppression of the lateral growth plane, i.e. the (10 $\bar{1}$ 0) plane, to achieve a well-defined ZnO NW structure. Therefore, understanding the nucleation on the crystal plane of ZnO is very crucial for morphological control^{11,12}.

Moreover, the biggest challenge that needs to be overcome for the realization toward ZnO-based electronic devices is the fabrication of a stable p-type ZnO NW. ZnO NW is generally formed of an n-type semiconductor due to the self-compensating effect from native defects, for example, oxygen vacancy and interstitial Zn atoms¹⁴⁻¹⁶. There has already been a great deal of efforts on the fabrication of p-type ZnO films by the substitution of group-IA elements (Li, Na and K) and group-IB elements (Cu and Ag) on the Zn-sites^{17,18}. Although

significant progress has been made recently, the full control over the conductivity type is still to be obtained, and hence a comprehensive investigation of the fundamental properties of acceptors in ZnO is needed.

On the other hand, with the frontiers of electronics racing towards foldable, portable devices, there is an earnest search for flexible electronic components. ZnO NW on flexible substrate, such as plastic and polymer film seems increasingly important and has made great process in harvesting energy from mechanical movement^{19,20}. However, a great challenge here is the low melting points of such substrates, and the non-crystallinity of the polymer substrate, which results in a difficulty to a realization of a well-defined ZnO NW on flexible substrate. Moreover, to apply the ZnO NW-based flexible substrate to the energy harvesting application, which scavenges mechanical energy from our living environment and human body to produce electricity through electrification and electrostatic induction mechanism, the robust, durability and flexible ZnO NW are desirable.

In this study, to comprehensively understand the morphology control of ZnO NW, the growth of ZnO NW via seed-assisted hydrothermal was systematically studied through the effect of ZnO seed layer and the concentration of ZnO NW precursor. Secondly, to fully control the conductivity of ZnO NW, the electrical property of ZnO NW was modified by Ag doping via seed-assisted hydrothermal process with different concentrations of silver nitrate, which acts as a dopant precursor. Next, to realize the mechanically robust, durability and flexible ZnO NW-based device, the stretchable ZnO NW array on ZnO-embedded polymer was demonstrated by two-step growth of ZnO NW on rigid and polymer, respectively. Finally, the stretchable ZnO NW array on ZnO-embedded polymer was demonstrated as novel flexible devices. The stretchable ZnO NW array was assembled into nanogenerator to enhance the converting electrical output of triboelectric device through piezoelectric effect as called piezo-induced triboelectric (PIT) device. Furthermore, the potential use of the stretchable ZnO NW array on ZnO-embedded polymer as a flexible gas sensor was also demonstrated.

1.2 Objectives of the study

- 1.2.1 To control the morphology of ZnO NW via seed-assisted hydrothermal.
- 1.2.2 To control the conductivity of ZnO NW by Ag doping via seed-assisted hydrothermal.
- 1.2.3 To synthesize the stretchable ZnO NW array on ZnO-embedded polymer by two-step growth.
- 1.2.4 To demonstrate the flexible device based on the stretchable ZnO NW array on ZnO-embedded polymer; nanogenerator and gas sensor.

1.3 Scope of the study

- 1.3.1 Morphology control of ZnO NW via seed-assisted hydrothermal: ZnO seed layer was prepared via a sol-gel technique with different annealing temperatures. ZnO NW was synthesized via hydrothermal process with different concentrations of precursor. The synthesized seed layer and ZnO NWs were characterized by atomic-force microscope, X-ray diffractometer, scanning electron microscope and transmission electron microscope.
- 1.3.2 Conductivity control of ZnO NW via Ag doping: Ag-doped ZnO NW was synthesized via hydrothermal process with different concentrations of silver nitrate. The synthesized Ag-doped ZnO NWs were characterized by atomic-force microscope, X-ray diffractometer, scanning electron microscope, transmission electron microscope, energy-dispersive X-ray spectroscopy and X-ray photoelectron spectroscopy.
- 1.3.3 Synthesize the stretchable ZnO NW array on ZnO-embedded polymer: The ZnO NW was synthesized on Si substrate via seed-assisted hydrothermal. The ZnO NW was peeled off from Si substrate using PDMS, resulting in the ZnO-

embedded PDMS. The ZnO-embedded PDMS was subsequently used as a substrate for the second ZnO NW growth, in which the embedded ZnO NW acts as a seed for seed-assisted hydrothermal. The optimum concentration of ZnO precursor for the second hydrothermal growth was investigated. The synthesized ZnO NWs were characterized by X-ray diffractometer and scanning electron microscope.

1.3.4 Demonstration of the flexible device based on the stretchable ZnO NW array on ZnO-embedded polymer:

1.3.4.1 Demonstration of a hybrid nanogenerator to enhance a converting electrical output of triboelectric device through piezoelectric effect from ZnO NW

1.3.4.2 Demonstration of a gas sensor toward ethanol methanol and acetone detection.

The summary of the study scope is shown in Figure 1.1

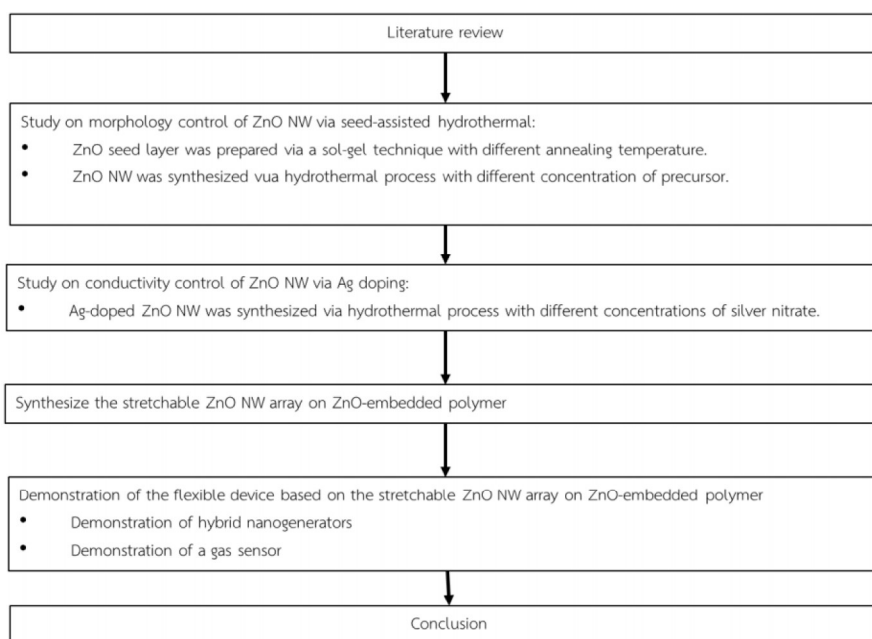


Figure 1.1 The summary of the study scope.

1.4 Expected Results

- 1.4.1 ZnO seed with a high crystallinity in the plane of (002) and a well-defined ZnO NW with a controllable morphology.
- 1.4.2 Ag-doped ZnO NW with a controllable morphology and a controllable Ag concentration.
- 1.4.3 Stretchable ZnO NW on ZnO-embedded polymer with a mechanically robust, durability and flexibility
- 1.4.4 Successful demonstration of the ZnO NW-based flexible devices; a high performance nanogenerator and a gas sensor

CHAPTER 2

LITERATURE REVIEW AND THEORETICAL BACKGROUND

2.1 Zinc oxide

Zinc oxide (ZnO) is a wide band gap semiconductor ($E_g = 3.37$ eV) of the II-VI group, naturally n-type semiconductor due to zinc interstitials and oxygen vacancies. ZnO is also biodegradable, biocompatible, and biosafe for medical and environmental applications. There are two main forms of ZnO crystal, cubic zinc blende and hexagonal wurtzite as shown in Figure 2.1. In general condition, ZnO exhibits a hexagonal wurtzite structure with lattice constants as follows; $a = 0.325$ nm, $b = 0.325$ nm, and $c = 5.20$ nm. A large exciton binding energy (60 meV) of ZnO make in be a candidate material in many applications such as lasers, light emitting diodes, solar cells, and photodetectors^{21,22}. The properties of ZnO are summarized in Table 2.1.

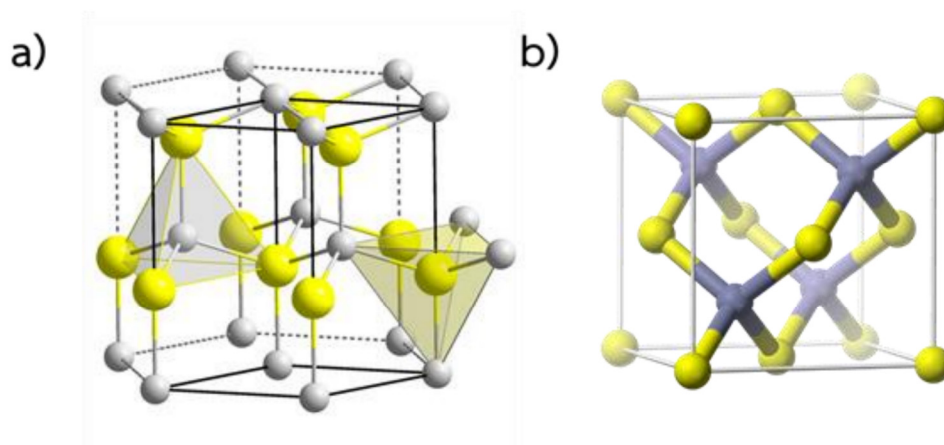


Figure 2.1 ZnO structure (a) the wurtzite structure model (b) the zinc blende unit cell²³.

Table 2.1 ZnO properties

Properties of ZnO	Value
Molecular weight	81.38 g/mol
Density	5.606 g/cm ³
Melting point	1,975 °C (2,248 K) (decomposition)
Band gap	3.3 eV
Exciton binding energy	60 meV
Crystal structure	Wurtzite / Cubic
Lattice constant	a = b = 3.25 Å, c = 5.2 Å

2.2 Zinc oxide nanowire

ZnO has many different structures depending on the conditions of synthesis (precursors, synthesis techniques, temperature and time) such as ZnO nanowires (NWs), ZnO nanoparticles, ZnO nanoflowers, ZnO nanobelts, ZnO nanoplate and ZnO nanotubes as shown in Figure 2.2. In this work, we have focus on ZnO NW structure. ZnO NWs is one-dimension material with a diameter of nanometer (10-100 nanometers) but have a length in the micrometer scale. ZnO NWs are commonly used in nanoelectronics device applications such as gas sensors, nanogenerators and solar cells as shown in Figure 2.3-2.5, respectively. ZnO NWs are semiconductors with a wide energy gap, which can be controlled from the size of the NWs, also have high exciton binding energy (60 meV), high temperature and high voltage resistance, and higher surface area per volume than thin films and bulk material structure^{24,25}.

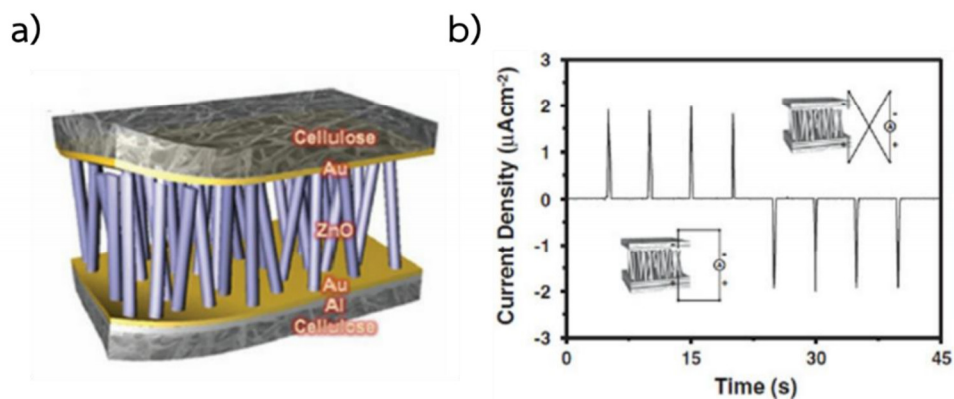


Figure 2.4 ZnO NWs-based nanogenerator (a) Schematic view of ZnO NWs nanogenerator. (b) Short circuit current measurement of ZnO NWs-based nanogenerator ²⁷.

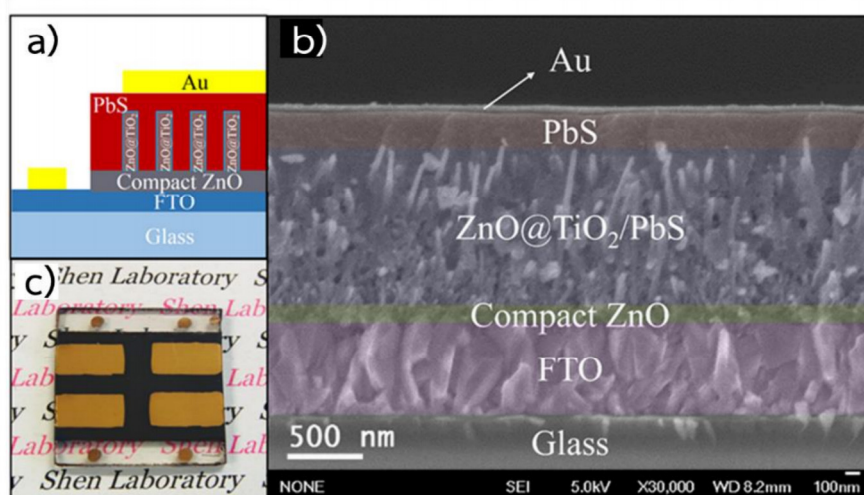


Figure 2.5 ZnO NWs-based solar cells (a) A schematic of the solar cell with ZnO NWs heterojunctions, (b) A photograph of standard solar cells. (c) Cross-section SEM image of the ZnO NWs-based solar cells ²⁸.

2.2.1 Synthesis of zinc oxide nanowire

Synthesis of ZnO NWs can be divided into two main methods. The first method is metal catalyst assisted growth and the other one is metal catalyst free.

2.2.1.1 Metal catalyst assisted growth

Vapor liquid solid growth (VLS growth) is a gas phase synthesis method. In VLS growth, the metal is required to be used as a catalyst to form a nanowire structure²⁹. Commonly used catalysts are such as gold, copper, platinum, tin, silver, nickel, etc. The advantage of this method is that it can easily control the size, position, density of ZnO NWs with high crystallinity. But disadvantages are catalyst residue, high temperature requirements, vacuum requirements and expensive system. The mechanism of VLS growth First, a thin metal film (catalyst) is deposited onto a substrate by sputter deposition or thermal evaporation. The substrate is annealed at high temperatures for forming metal-Si alloy droplets on the substrate surface (the thick of metal film effects to larger droplets). Second, one-dimensional crystalline NWs are then grown by a liquid metal-alloy droplet-catalyzed chemical or physical vapor deposition process, which takes place in a vacuum deposition system. Metal-Si droplets on the surface of the substrate act to lower the activation energy of normal vapor-solid growth. Finally, ZnO precursor is diffused and is accumulated in metal-Si droplets until the solution is saturated to form a solid crystalline (ZnO NWs) as shown in Figure 2.6.

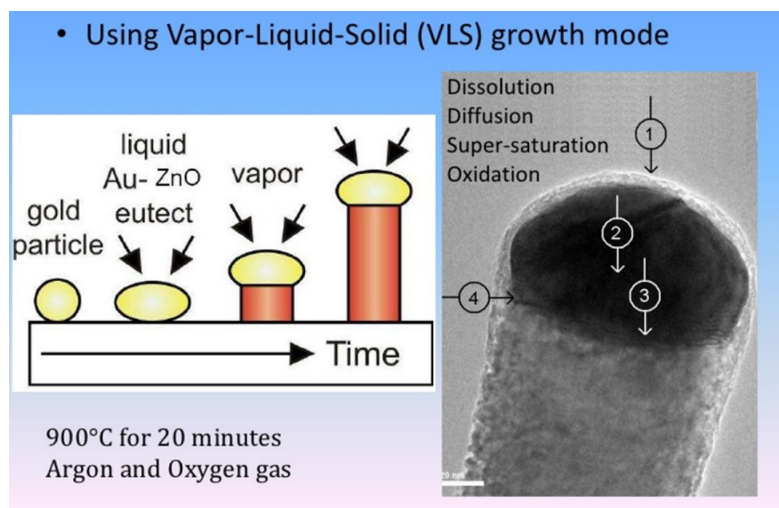


Figure 2.6 The schematic view of VLS growth³⁰.

2.2.2.2 Metal catalyst-free growth

In metal catalysts free, growth a thin film of ZnO is required to act as a seed layer. Nucleation and growth was easier when using the seed layer. Since of the seed Layer has a lower activation energy than other areas in the system. The advantage of the seed layer is that the size, density and position of the NWs can be controlled by the seed layer and the catalyst does not remain in the system. The synthesis of ZnO NWs using seed-assisted hydrothermal techniques is widely used, due to its low-temperature synthesis below 100 ° C as shown in Figure 2.7, which is suitable for a use in flexible substrate, easy and uncomplicated instrument, low cost, high crystallinity, and easily morphology control by using the concentration of precursor or synthesis time ¹¹⁻¹³. The general process for vertically aligned ZnO NWs grown on a substrate by the hydrothermal method is as follow.

1. A thin layer of ZnO seed layer on a substrate. The seed layer promotes nucleation for the growth of NWs due to the lowering of the activation energy.
2. An alkaline reagent (such as NaOH or hexamethylenetetramine(HMTA)) and Zn²⁺ salt (such as Zn(NO₃)₂ and ZnCl₂.) aqueous solution is used as a precursor.
3. The ZnO seed substrate is kept in the growth solution at a certain temperature and a certain period of time.

In this work, zinc nitrate hexahydrate ((Zn(NO₃)₂·6H₂O) and HMTA were chosen as a precursor for the hydrothermal growth of ZnO NWs. The chemical reactions can be explained as the following equations

Decomposition reaction:



Hydroxyl supply reaction:



Supersaturation reaction:



ZnO NW growth reaction:



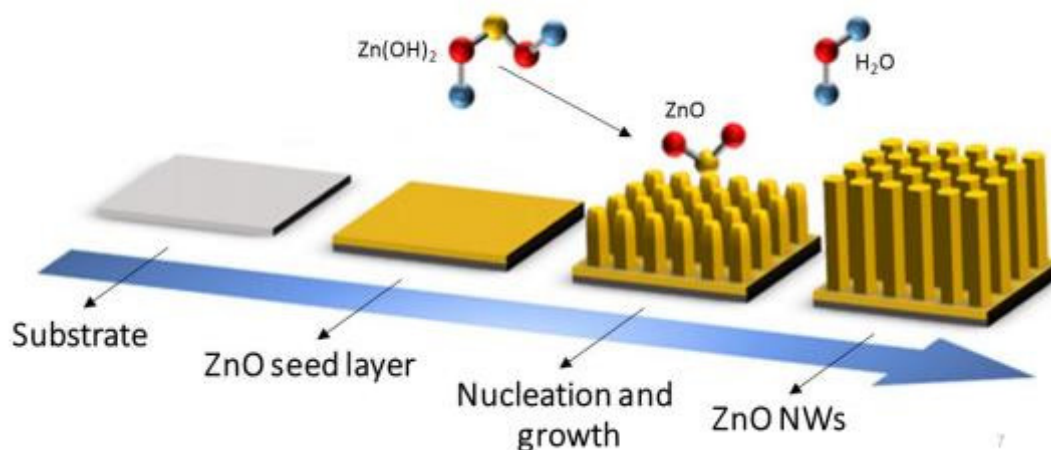


Figure 2.7 The schematic view of seed-assisted hydrothermal techniques.

2.3 Zinc oxide seed layer

As mentioned in Section 2.2.2.2, metal catalyst-free growth. ZnO seed layer is necessary. The seed layer helps to control the position of the nucleation and the growth of the ZnO NWs. In addition, it also controls the morphology of the ZnO NW. There are several methods to prepare ZnO seed. For example, sputtering and sol-gel methods are popular methods to prepare ZnO seed layer.

2.3.1 Sputtering technique

Sputtering techniques is widely used for a preparation of seed layer film thickness and crystal size is easily controlled by control power, pressure and time during sputtering. However, disadvantage are the high cost and the need of a vacuum system. To deposit a thin film, atoms in the target, source of a desired depositing material, are knocked off (sputtered out) by bombardment with neutral atoms, neutrons, positive ions, electrons, or phonons as shown in Figure 2.8. An overview of the sputtering system is shown Figure 2.9. After the bombardment, some kinetic energy was transferred from electron to target atom. As seen in the Figure 2.9, magnetics were equipped to enhancing sputtering yield (also called “RF-magnetron sputtering”) by increasing the probability of the collision between electrons and

gas molecules in the plasma via inducing electrons moving into helical path. It also lessens substrate damage caused by stray particles.

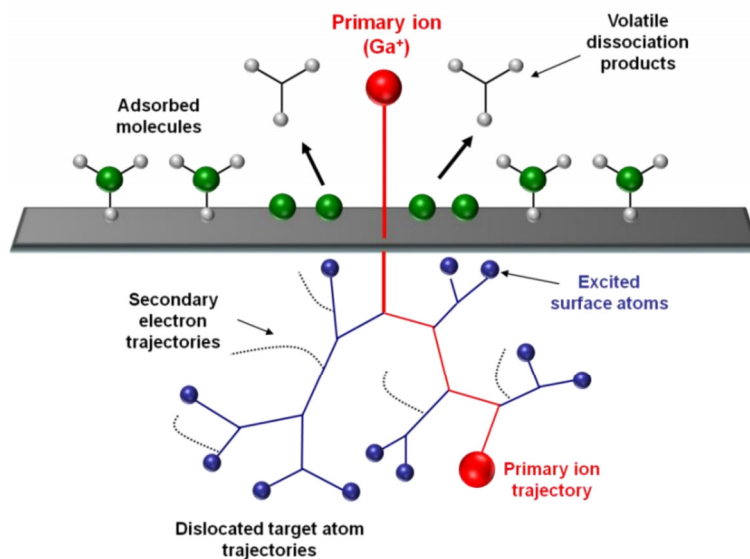


Figure 2.8 Sputtering of atoms from a target surface under the influence of incident ions.

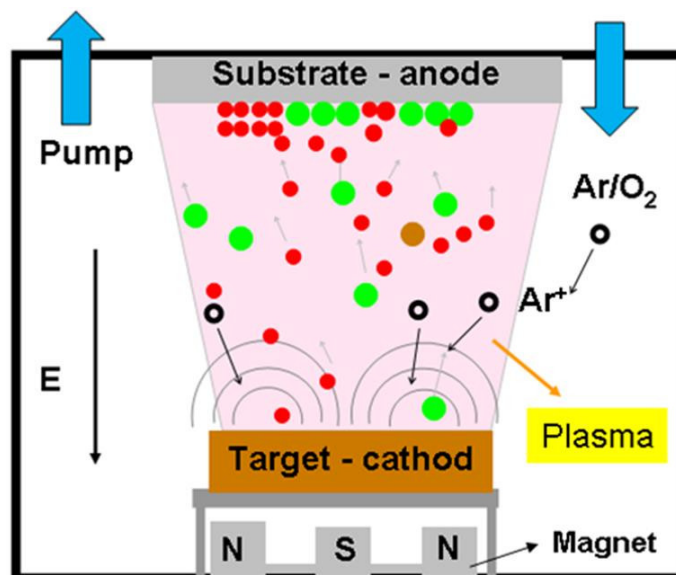


Figure 2.9 Schematic view of the sputtering system.

2.3.2 Sol-gel technique

Sol-gel technique is a synthesis technique in the form of a solution consisting of the following process:

1. Hydrolysis is a reaction involving the breaking of a bond in a molecule using water for decomposed the large molecule to small molecule.
2. Polymerization is a process of reacting monomer molecules together in a chemical reaction to form polymer chains.
3. Condensation reaction is the process by which two molecules react to form a covalent bond and with a loss of water molecule (H_2O) or alcohol ($R-OH$).
4. Nucleation and Growth ^{31,32}.

Conditions for ZnO seed layer synthesis by sol-gel technique is as follows.

1. Precursors in group of Zinc Salt, such as zinc acetate ($Zn(O_2CCH_3)_2$) or zinc nitrate ($Zn(NO_3)_2$)
2. Alcohol solutions such as ethanol (C_2H_5OH) or polyvinylalcohol (PVA; $[-CH_2CH(OH)-]_n$).
3. Additives are chemical species presenting at least one functional group, which enables these species to play several roles. They act as basic or acid and/or chelating agent such as monoethanolamine ($(HOCH_2CH_2)NH_2$) or diethanolamine ($(HOCH_2CH_2)_2NH_2$)
4. Time for polymer aging 24 - 72 hours

After the solution is left for 24-72 hours, it becomes a gel containing zinc hydroxide ($Zn(OH)_2$). Then, the gel is coated on the substrate, such as silicon or glass slide by spin coating technique and is heat from 150 – 850°C for a use as a seed layer as shown in Figure 2.10.

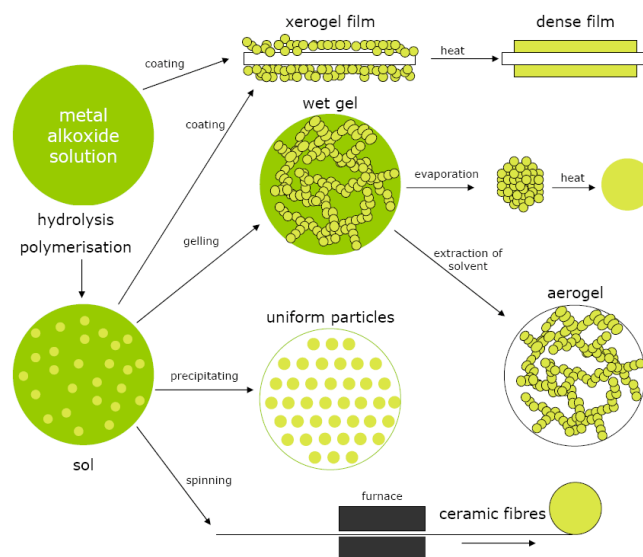


Figure 2.10 Schematic view of sol-gel process.

2.4 Nanogenerators

Nanogenerator is a technology that converts mechanical or thermal energy to electrical energy. A nanogenerator has three main types: piezoelectric, triboelectric, and pyroelectric nanogenerators. The piezoelectric and triboelectric nanogenerators convert mechanical energy into electricity, while the pyroelectric nanogenerators is used to harvest thermal energy into electricity³³.

2.4.1 Piezoelectric nanogenerator base on ZnO nanowire

Piezoelectric nanogenerator (PENG) is of great interest to many researchers because it can directly convert mechanical energy into electricity as shown in Figure 2.4. The breaking of symmetry in the crystal structure under external force is a key mechanism of electricity generation of piezoelectric materials as shown in Figure 2.11. This phenomenon is called piezoelectric potential. In this research piezoelectric property of ZnO NWs is focused. For the wurtzite-structured ZnO crystal, the charge center of the cations and anions overlaps with one another at undisturbed state. The symmetry is broken when an external force is applied. So, the cations and anions are separated and form an electric dipole, resulting in the formation of piezoelectric potential. When a piezoelectric material is connected to an external circuit, the free electrons are driven to flow through the external circuit in order to partially screen

the piezoelectric potential and achieve a new equilibrium state, which is the energy conversion process^{19,20,34,35}.

2.4.2 Triboelectric nanogenerator

Triboelectric nanogenerator (TENG) is invented recently, which could convert mechanical energy into electricity. TENG could be inherently flexible and meanwhile serves as an energy source for portable or implantable electronic device, or as one of self-powered environmental device. The fundamental working principle of TENG is a conjugation of contact electrification and electrostatic induction. Contact electrification provides static polarized charges and electrostatic induction is the main mechanism that converts mechanical energy to electricity as shown in figure 2.12. The work principle can be explained as follows : (I) At initial state, no charge is induced on two polymers surfaces, with no electric potential difference between the two electrodes. (II) When an external force applied, the two polymers are brought into contact with each other. The charge is induced on both of polymers surfaces due to triboelectric effect. According to the triboelectric series that is a list of materials based on their tendency to gain or lose charges as shown in Figure 2.13, electrons are injected from polymethylmethacrylate (PMMA) into kapton, resulting in net negative charges at the kapton surface and net positive charges at the PMMA surface, respectively. (III) while external force is releasing, the PMMA separates from kapton surface. Accordingly, a potential difference is established between the two electrodes. (IV) As the two polymers are released, potential difference is reaching an electrostatic equilibrium. (V) When the two polymers are compressed again, the electrostatic equilibrium in triboelectric device is broken, resulting in a difference in potential again³⁶⁻⁴⁰.

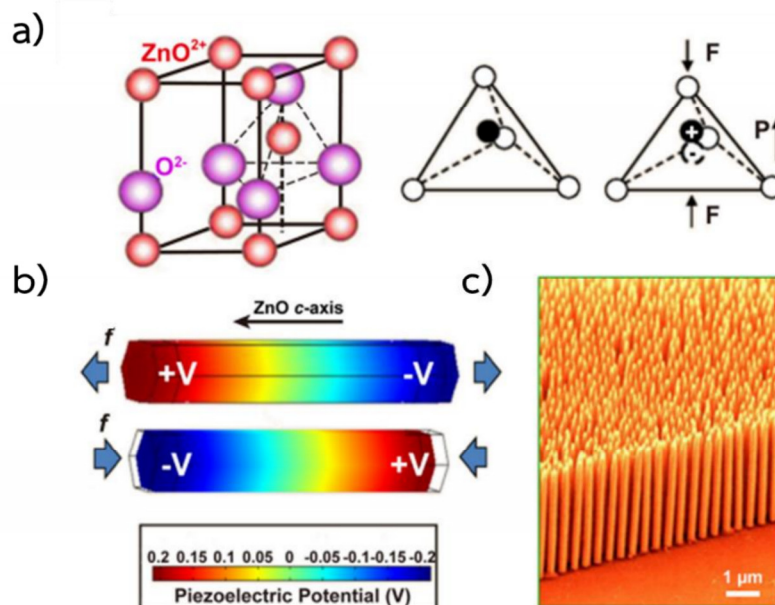


Figure 2.11 (a) Piezoelectric model of wurtzite-structured ZnO. (b) Piezopotential of a stretched ZnO NWs. (c) SEM image of ZnO NWs⁴¹.

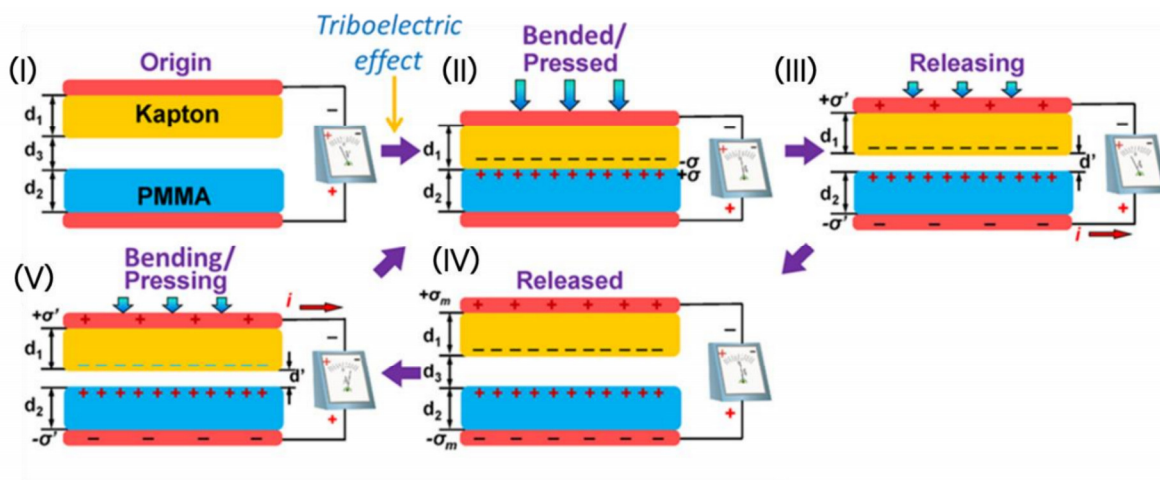


Figure 2.12 Working principle of Vertical contact-separation mode of triboelectric nanogenerator.

The table lists materials in two columns. To the left of the table is a vertical color scale from blue at the bottom to red at the top, with an upward-pointing arrow labeled 'Positive'. To the right is a similar color scale with a downward-pointing arrow labeled 'Negative'. The materials are arranged from most positive at the top to most negative at the bottom.

Polyformaldehyde 1.3-1.4	(continued)
Etylcellulose	Polyester (Dacron)
Polyamide 11	Polyisobutylene
Polyamide 6-6	Polyuretane flexible sponge
Melanime formol	Polyethylene Terephthalate
Wool, knitted	Polyvinyl butyral
Silk, woven	Polychlorobutadiene
Aluminum	Natural rubber
paper	Polyacrilonitrile
Cotton, woven	Acrylonitrile-vinyl chloride
Steel	Polybisphenol carbonate
Wood	Polychloroether
Hard rubber	Polyvinylidene chloride (Saran)
Nickel, copper	Polystyrene
Sulfur	Polyethylene
Brass, silver	Polypropylene
Acetate, Rayon	Polyimide (Kapton)
Polymethyl methacrylate (Lucite)	Polyvinyl Chloride (PVC)
Polyvinyl alcohol	Polydimethylsiloxane (PDMS)
(continued)	Polytetrafluoroethylene (Teflon)

Figure 2.13 Triboelectric series for materials following a tendency to easily lose electrons (positive) and to gain electrons (negative)

2.5 Gas sensors

Semiconducting metal oxides have been considered as promising candidates for gas-sensing applications because of their high sensitivity, easy fabrication methods, low cost, and high compatibility with other parts and processes as shown in Figure 2.3. Different types of metal oxide such as ZnO, SnO₂, TiO₂, In₂O₃, WO₃, TeO₂, CuO, CdO, Fe₂O₃, and MoO₃ have been developed and employed in the fabrication of gas sensors and it was found that chemical components, surface state, morphology, and microstructure play important roles in gas-sensing performance. Metal oxide gas sensors depend on changes of electrical conductivity due to the interaction with the surrounding atmosphere. The normal working temperature of metal oxide gas sensors is within the range between 200°C and 500°C. The working temperature should be high enough so that gas reactions occur in a time on the order of the desired response time and should also be low enough to avoid any variations in the

bulk of the sensing matrix. The single crystal structure synthesized at temperatures higher than the operating temperature of the sensor shows high stability. Sensing response (resistance increase or decrease) leads to a simple classification types of gas. Gas can be classified as oxidizing or reducing and metal oxides can also be classified as p-type or n-type. In p-type show a resistance increase in the presence of traces of reducing gases and resistance decrease to oxidizing gases, while n-type oxides show opposite behaviors ^{42,43}.

2.5.1 Gas sensors based on ZnO nanowire

ZnO NWs is one of the earliest discovered and most widely used metal oxide gas sensing materials. ZnO NWs gas sensors use a chemical sensitivity of the surface to different adsorbed gases, which cause a change in a resistance of the sensor. Large surface area of the NW structure is a key for the sensitivity and response time of ZnO NWs gas sensors. There are many gases and vapors that can be detected by ZnO NWs, such as NO, NO₂, CO, NH₃, H₂, O₂, and ethanol, methanol and acetone ^{6,26}.

CHAPTER 3

MORPHOLOGY CONTROL OF HYDROTHERMAL ZINC OXIDE NANOWIRES

The morphology of ZnO NWs can be controlled in several ways. In this research, the morphology of ZnO NWs was controlled by ZnO seed layer and precursor concentration. The ZnO seed layer could control the alignment of ZnO NWs, while the precursor concentration could control the morphology of ZnO NWs.

3.1 Synthesis of ZnO nanowires by seed-assisted hydrothermal

3.1.1. Synthesis of ZnO seed layer

The ZnO seed layer was prepared by sol-gel process as follows;

- (1) The precursor of ZnO seed was prepared by mixing polyvinyl alcohol (PVA, $[\text{CH}_2\text{CH}(\text{OH})]_n$) and DI water by a weight ratio of 0.08:1 and stirring at 80°C for 1 h.
- (2) 0.1 g of zinc acetate dehydrate ($\text{Zn}(\text{CH}_3\text{COO})_2$) was added into the above solution and continuously stirred at room temperature for 2 h and aged at room temperature for 24 h.
- (3) The precursor of ZnO seed was coated on Si (100) substrate. Prior coating, the Si substrate was cleaned by acetone, isopropanol and DI water in ultrasonic bath for 10 min, respectively.
- (4) The sol of ZnO seed was spin-coated onto the Si substrates at 3000 rpm for 5 min. The zinc acetate molecule was well dispersed in PVA matrix on the Si substrate.
- (5) The ZnO-seed coated Si substrate was subsequently heated at difference temperatures from 100°C to 600°C for 3 h to optimize the temperature to remove organic molecules and to form ZnO nanoparticles, which act as nucleation sites for the growth of ZnO nanowire.
- (6) The morphology and the crystallinity of the ZnO seed layer were characterized by atomic force microscope (AFM) and X-ray diffractometer (XRD), respectively.

3.1.2 Synthesis of ZnO nanowires by ZnO seed layer

ZnO NW was synthesized by hydrothermal using the seed layer prepared by the method described in section 3.1.1. The growth procedure is described as follows;

- (1) The ZnO precursor for hydrothermal process was prepared. Zinc nitrate hexahydrate ($\text{Zn}(\text{NO}_3)_2 \cdot 6\text{H}_2\text{O}$) and hexamethylenetetramine ($\text{C}_6\text{H}_{12}\text{N}_4$) were mixed by a weight ratio of 1:1 in DI water and were stirred at room temperature for 4 h. To study the effect of precursor concentration on ZnO morphology, different precursor concentrations ranging from 5 to 100 mM were prepared.
- (2) The ZnO-seed coated Si substrate (prepared from section 3.1.1) was immersed upside down into the precursor solution in a sealed beaker with a typical growth temperature of 95°C for 3 h. The ratio of the area of ZnO seed (cm^2) to the volume of the ZnO NW precursor solution (ml) is 1:50.
- (3) The morphology, and the crystallinity of the ZnO NWs were characterized by SEM and XRD, respectively.

3.2 Effect of ZnO seed layer on morphology of ZnO NWs

Figure 3.1 shows an XRD spectrum of ZnO seed layer after annealing at different temperatures from 100°C to 600°C. Zinc acetate at the peak position of 47.8° was observed at 100°C and 300°C. At 400 °C, the zinc acetate peak at 47.8° was not observed, but we found the ZnO (101) plane at a position 36.1°. While 500°C and 600 °C, the ZnO peaks of (101) and (002) planes were found at positions of 36.1° and 34.6°, respectively. The results imply that zinc acetate decomposes into ZnO (101) plane at 400°C and re-crystallization to ZnO (002) plane at 500°C -600°C. The FWHM of the ZnO (002) plane annealed at temperature of 600 °C was less than that of temperature of 500 °C, which represents higher crystallinity in the ZnO (002) plane of temperature of 500 °C.

Figures 3.2(a) - 3.2(c) show AFM images of the ZnO seed layer after annealing at different temperatures from 400°C to 600°C. The annealing temperature affects the

morphology of the ZnO seed layer. The higher temperature results in a larger particle size and crystalline size of ZnO seed layer are larger and a higher RMS roughness as shown in Table 3.1.

Figures 3.3(a) - 3.3(f) show SEM images of ZnO NWs from ZnO seed layers annealed at different temperatures of ZnO seed layers from 400°C to 600°C by hydrothermal process. It was found ZnO seed layers annealed at different temperatures result in affect to different morphologies of ZnO NWs

Figure 3.4 shows the relationship between the size of ZnO NWs and the size of the ZnO seed particles compared to the annealing temperature of the ZnO seed layer and Figure 3.5 shows the relationship between the densities of ZnO NWs and ZnO seed particles. The results show that the sizes of ZnO NWs were 72.6 ± 11.4 , 99.1 ± 13.4 , 114.1 ± 25 and the sizes of ZnO seed particles were 26.8 ± 5.2 , 32.1 ± 6.8 and 45.3 ± 13.1 nm and the densities of ZnO NWs were 6.3×10^9 , 5.0×10^9 and 4.7×10^9 wire/square centimeters and the ZnO densities of the ZnO seed particle were 9.5×10^{10} , 5.7×10^{10} and 4.9×10^{10} particle/square centimeters, corresponding to annealing temperature of 400, 500 and 600°C, respectively. It was found that when the temperature increased, the densities of ZnO NWs and ZnO seed particles were decreased and when the temperature increased, the size of ZnO NWs and the size of ZnO particles was increased. It was found that the characteristics of ZnO NWs depend on two main factors:

1. Uniformity of the particle size of ZnO seed layer Compared to the ZnO NWs obtained from the ZnO seed layer at 400°C, 500°C and 600°C, it was found that the distribution of particle size of the ZnO seed was relatively narrow at 400°C and 500°C resulting in distribution a uniformity of ZnO NWs. In contrast, the distribution particle size of the ZnO seed was relatively wide wite irregular shapes and large standard deviation value at 600°C, resulting in a non-uniformity of ZnO NWs.

2. Crystallinity of ZnO seed in (002) plane. Although the annealing temperatures at 400°C and 500°C result in uniformity of ZnO NW morphology, but ZnO NWs synthesised by using the ZnO seed layer annealed at 400°C show poor orientation due to a low crystallinily of ZnO crystals in the (002) plane. While ZnO NWs synthesized by using the ZnO seed layer

annealed at 500 has a good orientation due to a high quality of ZnO crystallinity in the (002) plane.

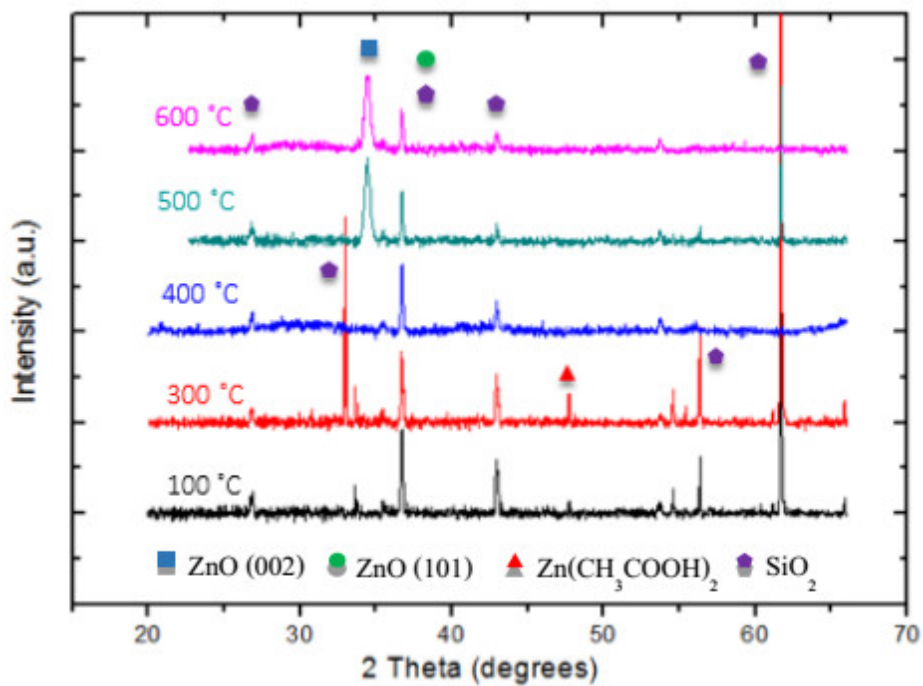


Figure 3.1 XRD spectrum of ZnO seed layer annealed a different temperatures from 100°C to 600°C

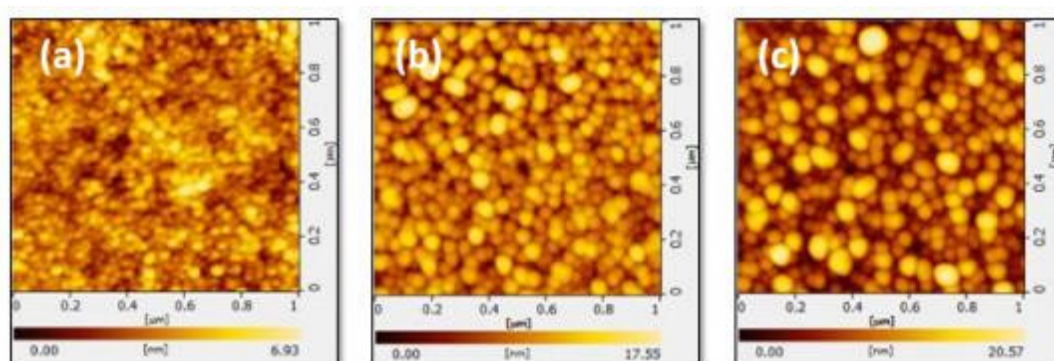


Figure 3.2 AFM images of ZnO seed layer annealed at (a) 400°C, (b) 500°C, and (c) 600°C.

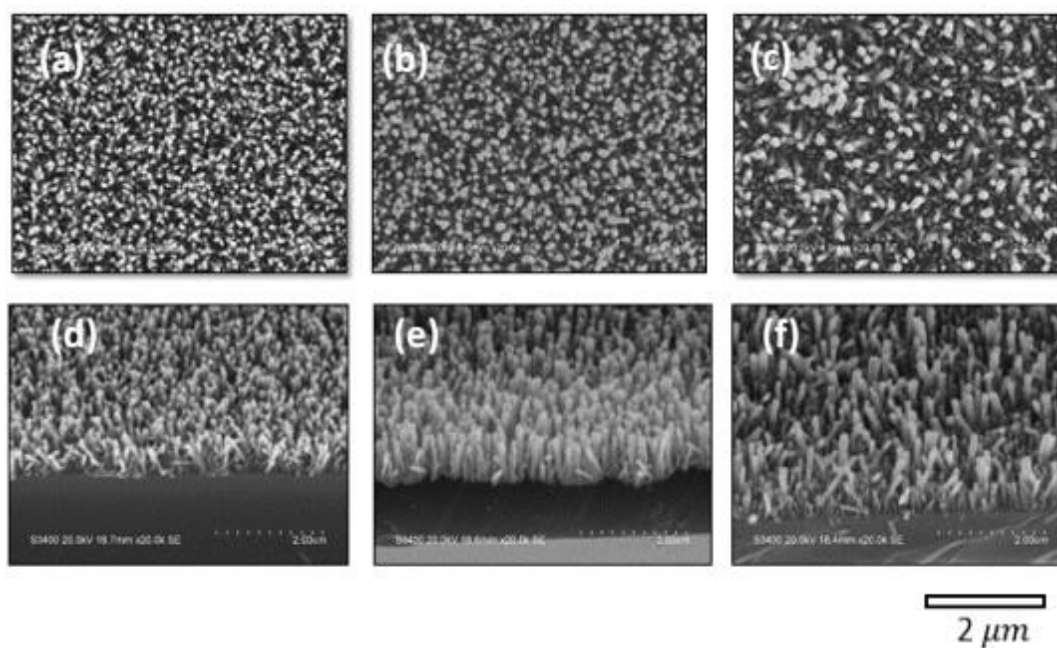


Figure 3.3 SEM images of ZnO NWs synthesized from ZnO seed layer annealed at (a) 400°C, (b) 500°C and (c) 600°C.

Table 3.1 Crystallinity and morphology of ZnO seed layer

Sample	FWHM(002)	Crystallite size (002) (Å ^o)	Particle size (nm)	RMS (nm)
400 °C	-	-	26.8 ± 5.2	1.12
500 °C	0.43	221.45	32.1 ± 6.8	2.96
600 °C	0.38	240.15	45.3 ± 13.1	3.72

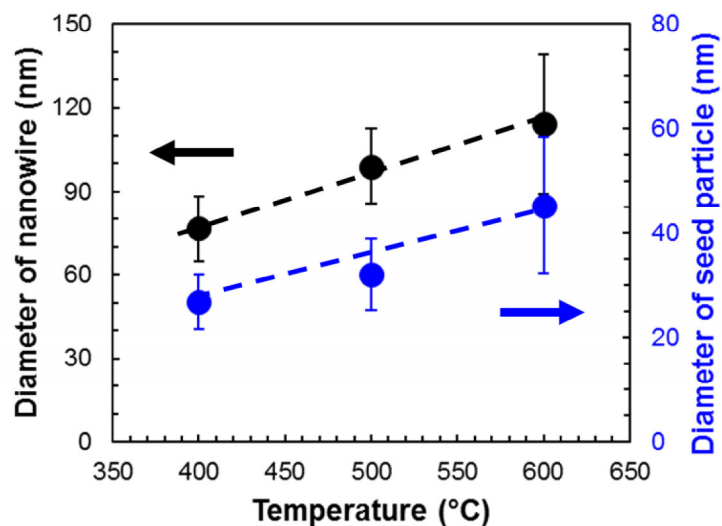


Figure 3.4 Relationship between the size of ZnO NWs and the size of the ZnO seed layer compared to the annealing temperature of the ZnO seed layer.

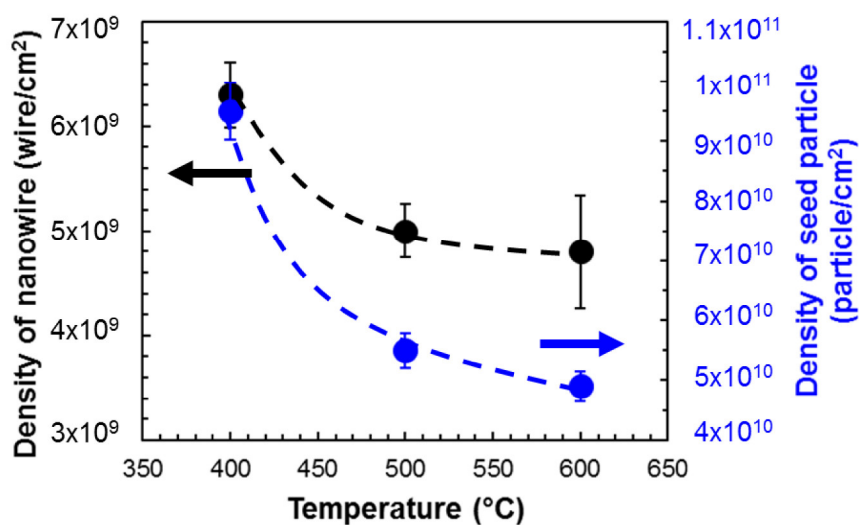


Figure 3.5 The relationship between the density of ZnO NWs and density of ZnO seed layer particle compared to annealing temperature of ZnO seed layer

3.3 Effect of ZnO precursor concentration on morphology of ZnO nanowires

Figure 3.6 shows SEM images of ZnO NWs synthesized by hydrothermal at different concentrations from 5 mM to 100 mM. It was found that the precursor concentration affected the size and density of ZnO NWs.

Figure 3.7 shows the relationship between the size and density of ZnO NWs to the ZnO precursor concentrations of 5, 10, 20, 40 and 100 mM. The size of ZnO NWs were 50 ± 13.3 , 108 ± 27 , 135 ± 38.2 , 259 ± 44 and 375 ± 65.9 nm respectively. The densities of ZnO NWs were 6.3×10^9 , 5.0×10^9 , 2.5×10^9 , 1.5×10^9 and 1.09×10^9 wire/square centimeter, respectively.

When the precursor concentration increases, the size of the ZnO NWs increases due to a high growth rate in the ZnO (100) plane and the evolution of ZnO NWs into thin films, as observed from a decrease in ZnO NWs density. To prove this hypothesis, an area fraction was calculated as shown in Figure 3.8. Area fractions of different ZnO precursor concentrations at 5, 10, 20, 40 and 100 mM were 12, 45, 36, 87 and 100 %, respectively. An increase in area fraction along with an increase in ZnO precursor concentration indicates that a high concentration results in a fast growth rate in ZnO (100) plane.

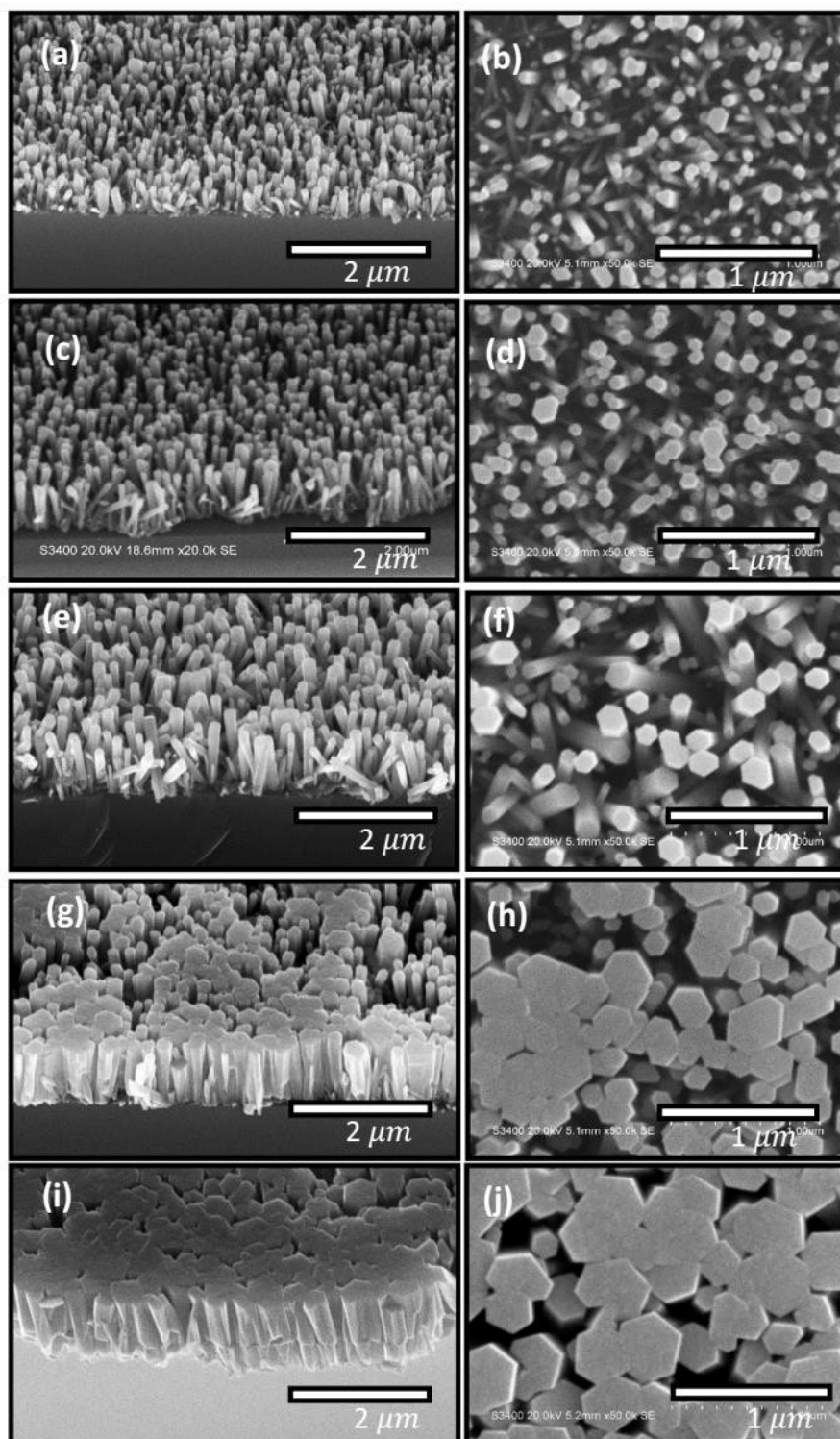


Figure 3.6 SEM images of ZnO NWs synthesized by hydrothermal with different concentrations from 5 mM to 100 mM.

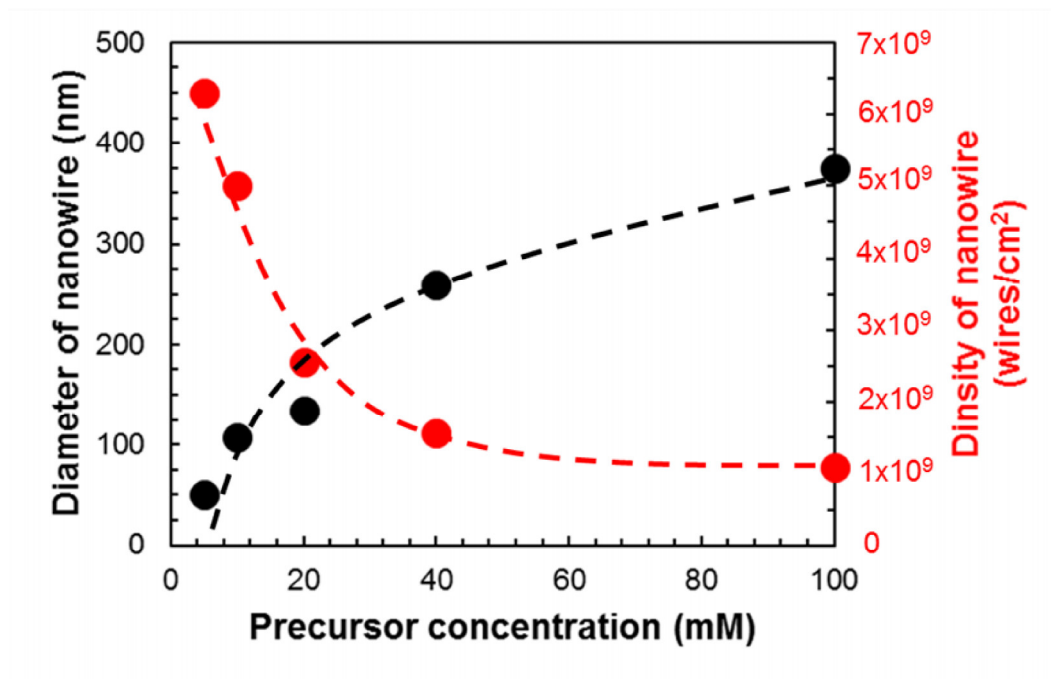


Figure 3.7 The relationship between the size and density of ZnO NWs to the ZnO precursor concentrations of 5, 10, 20, 40 and 100 mM.

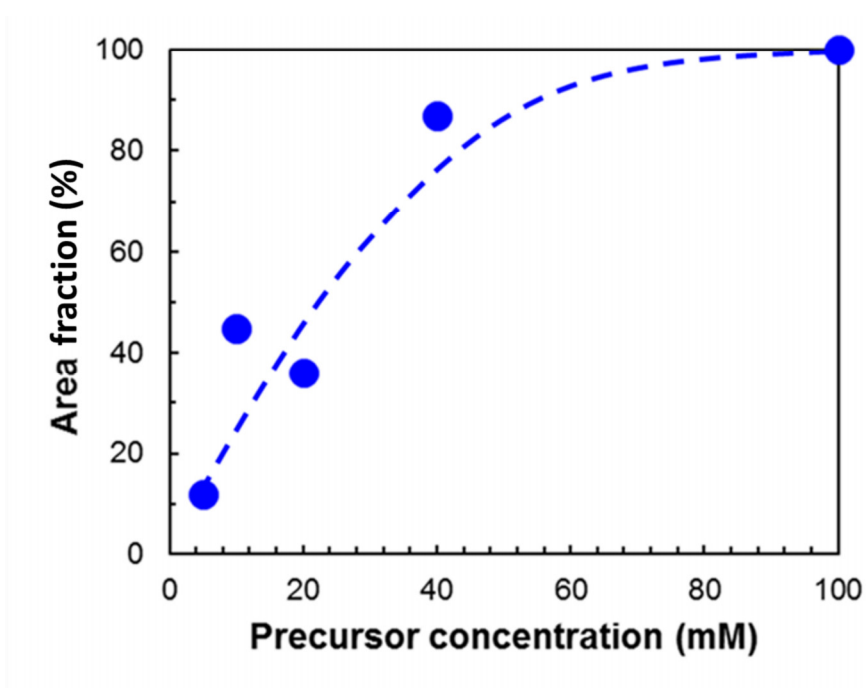


Figure 3.8 Area fraction of different ZnO precursor concentrations at 5, 10, 20, 40 and 100 mM.

CHAPTER 4

SYNTHESIS AND CHARACTERIZATION OF SILVER-DOPED ZINC OXIDE NANOWIRES

In this part, Ag-doped ZnO NWs with different dopant concentrations were studied.

4.1 Synthesis of Ag-doped ZnO Nanowires

4.1.1 Synthesis of ZnO seed layer

The ZnO seed layer was prepared by sol-gel process as follows;

- (1) The precursor of ZnO seed was prepared by mixing polyvinyl alcohol (PVA, $[\text{CH}_2\text{CH}(\text{OH})]_n$) and DI water by a weight ratio of 0.08:1 and stirring at 80°C for 1 h.
- (2) 0.1 g of zinc acetate dehydrate ($\text{Zn}(\text{CH}_3\text{COO})_2$) was added into the above solution and continuously stirred at room temperature for 2 h and aged at room temperature for 24 h.
- (3) The precursor of ZnO seed was coated on Si (100) substrate. Prior coating, the Si substrate was cleaned by acetone, isopropanol and DI water in ultrasonic bath for 10 min, respectively.
- (4) The sol of ZnO seed was spin-coated onto the Si substrates at 3000 rpm for 5 min. The zinc acetate molecule was well dispersed in PVA matrix on the Si substrate.
- (5) The ZnO-seed coated Si substrate was subsequently heated at difference temperatures from 100°C to 600°C for 3 h to optimize the temperature to remove organic molecules and to form ZnO nanoparticles, which act as nucleation sites for the growth of ZnO nanowire.
- (6) The morphology and the crystallinity of the ZnO seed layer were characterized by atomic force microscope (AFM) and X-ray diffractometer (XRD), respectively.

4.1.2 Synthesis of Ag-doped ZnO Nanowires by ZnO seed layer

Ag-doped ZnO NW was synthesized by hydrothermal using the seed layer prepared by the method described in section 3.1.1.1. The growth procedure is described as follows;

- (1) The ZnO precursor for hydrothermal process was prepared. Zinc nitrate hexahydrate ($\text{Zn}(\text{NO}_3)_2 \cdot 6\text{H}_2\text{O}$) and hexamethylenetetramine ($\text{C}_6\text{H}_{12}\text{N}_4$) were mixed by a weight ratio of 1:1 in DI water at the concentration of 10 mM.
- (2) Silver nitrate (AgNO_3) was then added to the ZnO precursor. To the study the effect of Ag ion concentration on the morphology of Ag-doped ZnO NWs, the AgNO_3 concentration was varied ranging from 0 to 1 mM. The precursor solution was subsequently stirred at room temperature for 4 h.
- (3) The ZnO-seed coated Si substrate (prepared from section 3.1.1) was immersed upside down into the precursor solution in a sealed beaker with a typical growth temperature of 95°C for 3 h. The ratio of the area of ZnO seed (cm^2) to the volume of the ZnO NW precursor solution (ml) is 1:50.
- (4) The morphology, internal structure, crystallinity and elemental composition with chemical state of the ZnO NWs were characterized by SEM, TEM, XRD and X-ray photoelectron spectroscope (XPS), respectively. The Photoluminescence measurements were also performed.

4.2 Characterization of Ag doped ZnO Nanowires

Figure 4.1 shows images SEM of ZnO NWs were synthesized by hydrothermal method at 10mM of ZnO precursor concentration and different concentration of AgNO_3 from 0 mM to 1 mM. It was that the concentration of AgNO_3 affects the morphology of ZnO NNs.

Figures. 4.2 – 4.4 shows the relationship between size, length and density of ZnO NWs with different concentration of AgNO_3 ranging from 0 to 1 mM, respectively. As the concentration increases, the size and length slightly change, while the density of the ZnO NWs drastically decreases. At AgNO_3 concentrations ranging 0.6 to 1 mM, ZnO was formed to thin

film structure. We explained that the formation of ZnO NWs was suppressed by increasing of Ag ion.

Figure 4.5 shows the results of EDX from TEM observation of individual ZnO NWs. The highest amount of Ag in ZnO NWs of 0.37 at% was found at 0.5 mM of AgNO_3 concentration. Here, it is necessary to elucidate the Ag doped ZnO NWs Ag^+ can substitute in Zn^{2+} site. XPS was used for analyzes the bonding of Ag^+ and substitution of Ag^+ in Zn^{2+} site as shown in Figure 4.6

Figure 4.6 show the Ag 3d XPS spectra of Ag doped ZnO NWs with different concentration of AgNO_3 ranging from 0 to 1 mM. It was found that the peak of Ag 3d shifts to the higher binding energy from 366.7 eV to 368.1 eV when higher AgNO_3 concentration. The shift to higher binding energy a lower electron density around Ag atom. This result indicates a bonding between Ag and oxygen atom. Especially, at 0.5 mM of AgNO_3 concentration, the peak of Ag_2O position at 367.9 indicate a successful substitute of Ag^+ into Zn^{2+} site to form Ag-doped ZnO.

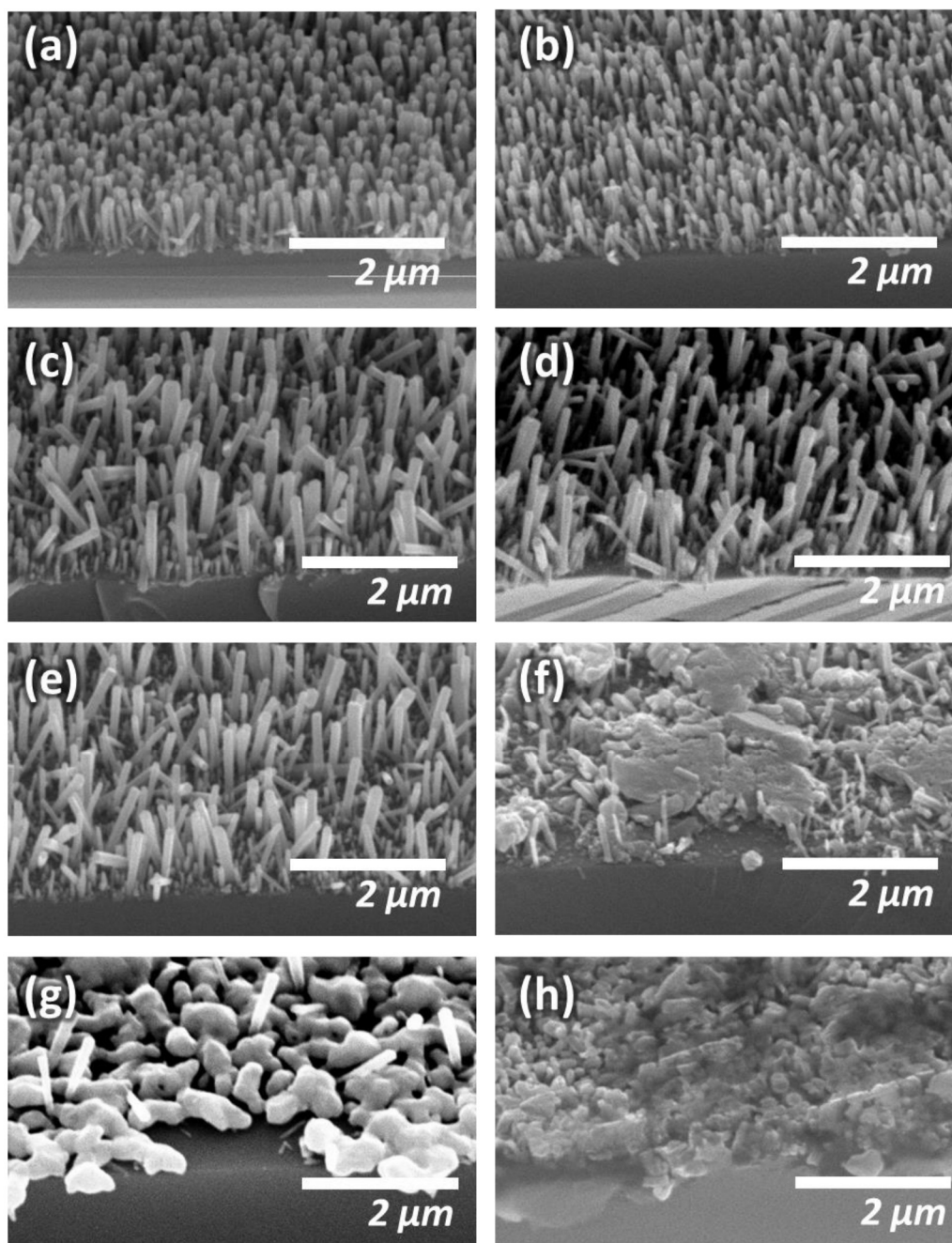


Figure 4.1 SEM images of ZnO NWs were synthesized by hydrothermal with different concentrations of AgNO_3 from 0 mM to 1 mM

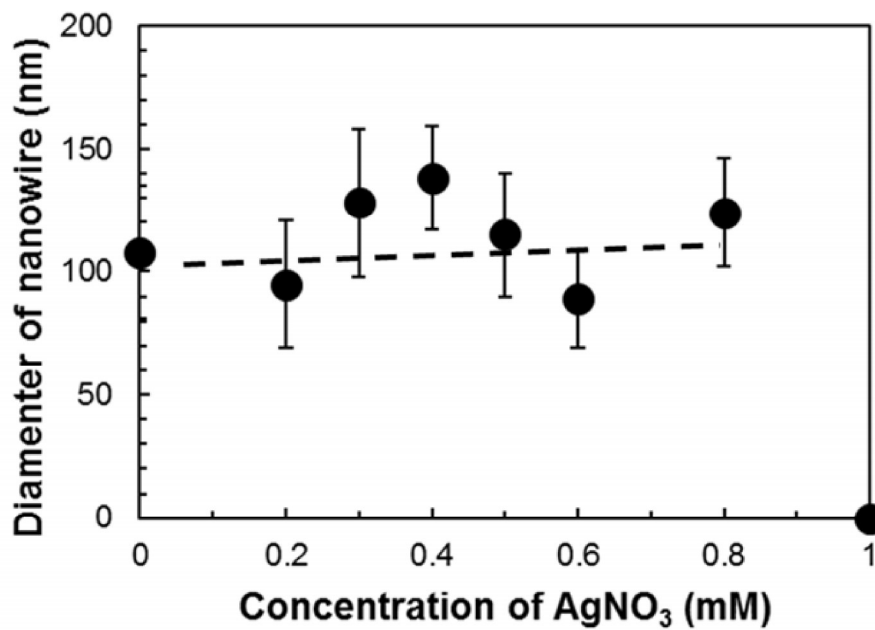


Figure 4.2 Relationship between size of ZnO NWs with different concentrations of AgNO₃ ranging from 0 to 1 mM.

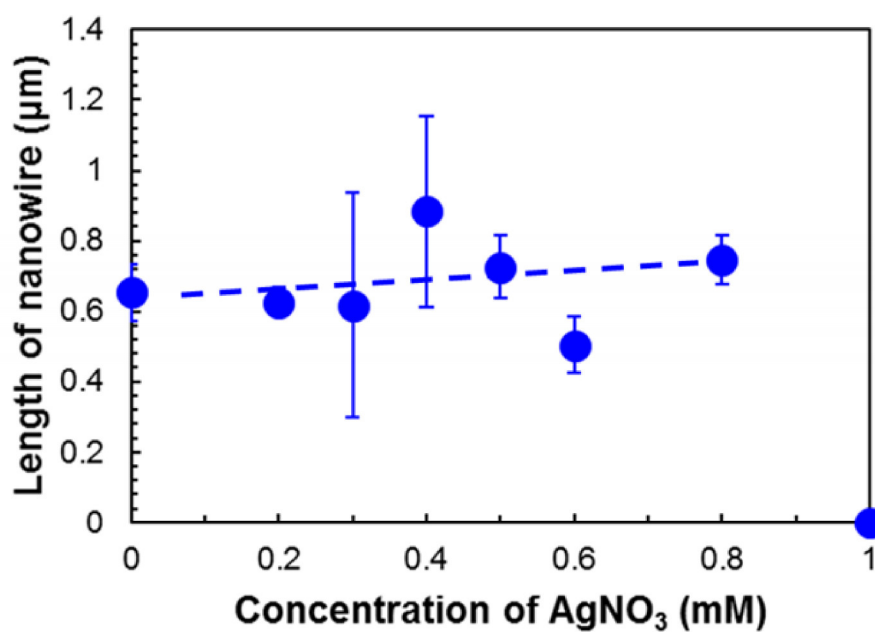


Figure 4.3 Relationship between length of ZnO NWs with different concentrations of AgNO₃ ranging from 0-1 mM.

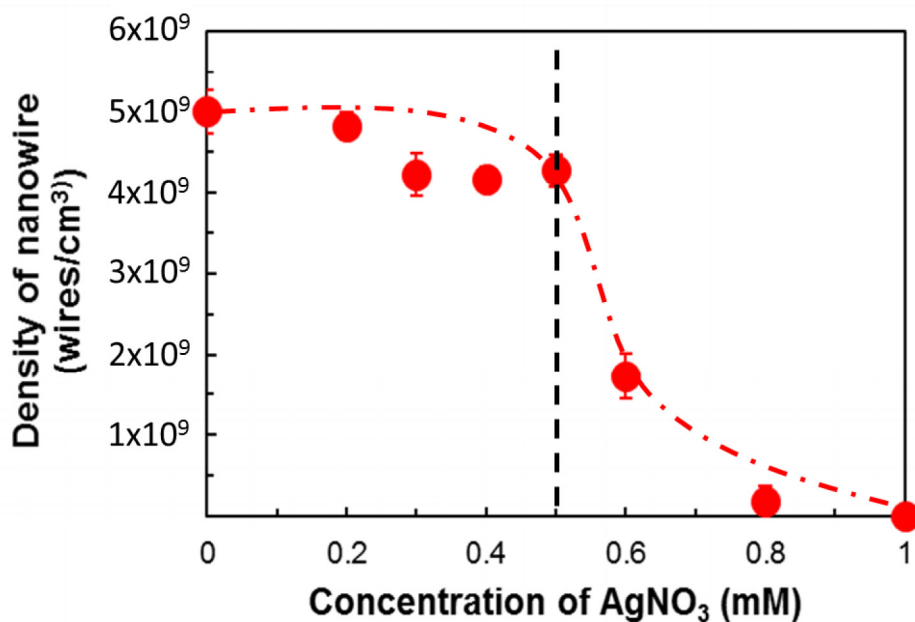


Figure 4.4 Relationship between density of ZnO NWs with different concentrations of AgNO₃ ranging from 0-1 mM

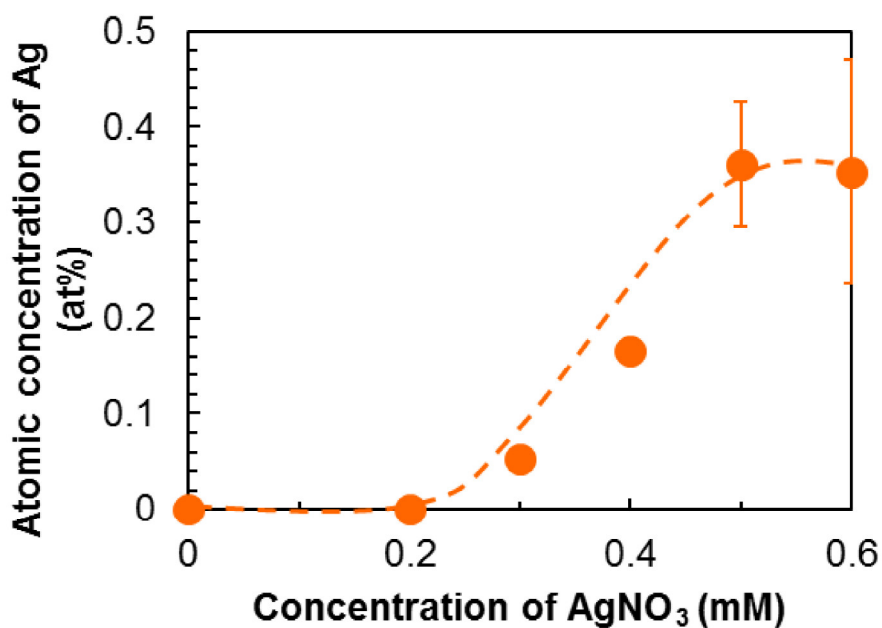


Figure 4.5 Relationship between Ag atomic concentrations of individual ZnO NWs with different concentration of AgNO₃ ranging from 0-0.6 mM. Characterized by TEM equipped with EDX.

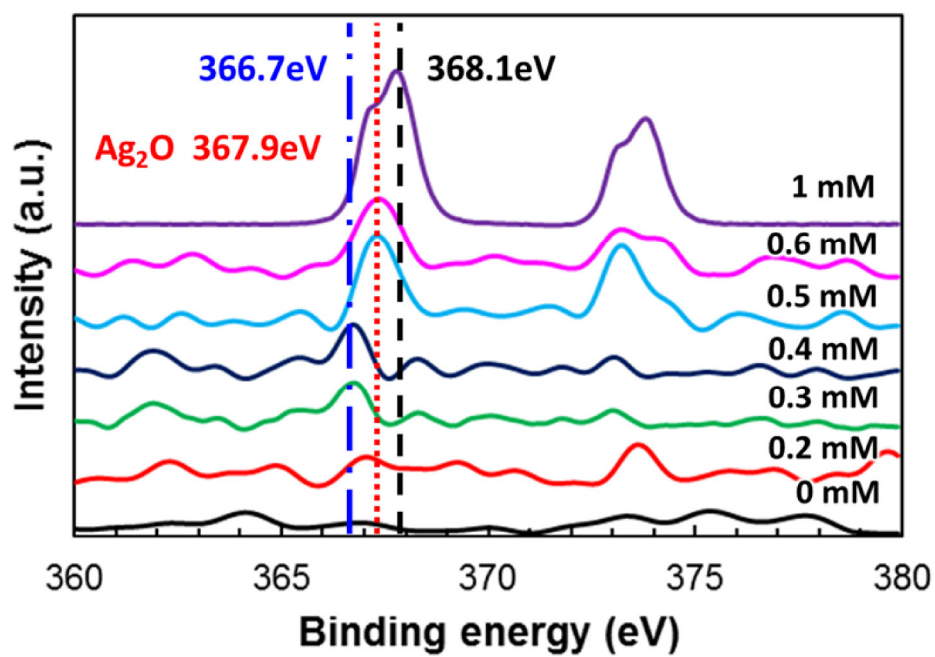


Figure 4.6 Ag 3d XPS spectra of Ag doped ZnO NWs with different concentration of AgNO₃ ranging from 0 to 1 mM.

CHAPTER 5

APPLICATION OF ZINC OXIDE NWS FOR FLEXIBLE NANODEVICES

A novel device structure was demonstrated to enhance a converting electrical output of triboelectric device through piezoelectric effect as called piezo-induced triboelectric (PIT) device. By utilizing the piezo-potential of ZnO NWs connected to the top Au electrode of Au/PDMS-Al triboelectric structure. Moreover the hydrothermal ZnO NEs was demonstrated as flexible gas sensor for VOC vapour detection

5.1 Synthesis of stretchable ZnO Nanowires on ZnO Nanowires-embedded polymer

The stretchable ZnO NWs on ZnO NW-embedded polymer was fabricated as follows;

- (1) ZnO NWs with the length of 2 μm were prepared by the same method as described in section 3.1 on 1.5×1.5 cm² of Si (100) substrate. This is the 1st step growth of ZnO NWs.
- (2) Polydimethylsiloxane (PDMS) was prepared by mixing the base and curing agent at a weight ratio of 10:1
- (3) PDMS (thickness of approximately 4 mm) was poured on the ZnO NW grown on Si substrate prepared from step (1).
- (4) PDMS was peeled out from Si substrate, resulting in a ZnO NW-embedded PDMS.
- (5) The ZnO NW-embedded PDMS could act as a seed for the 2nd growth of hydrothermal ZnO NWs. The ZnO NW-embedded PDMS was immersed upside down into the precursor solution as the same as the 1st growth. The effect of precursor concentration on the 2nd grown ZnO NW was investigated.
- (6) The morphology, internal structure and the crystallinity of the stretchable ZnO NW array on the ZnO-embedded PDMS were characterized by SEM and XRD,.

Figure 5.1 shows SEM image of ZnO NWs grown on ZnO NW-embedded PDMS after 2nd step growth.

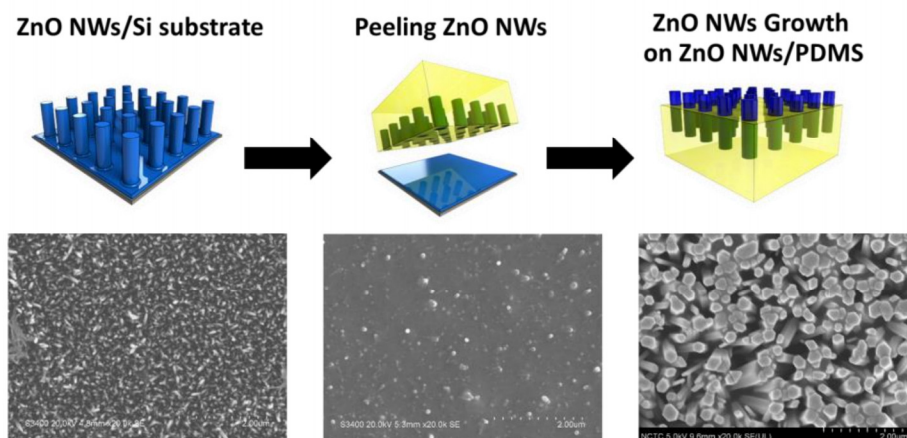


Figure 5.1 SEM images of ZnO NWs grown on ZnO NW-embedded PDMS after the 2nd step growth

5.2 Stretchable ZnO NW array for piezoelectric-induced triboelectric (PIT) device

5.2.1 Fabrication of stretchable ZnO NW array for piezoelectric-induced triboelectric (PIT) device

The fabricated stretchable ZnO NW array on ZnO NW-embedded PDMS was demonstrated as hybrid nanogenerator. The structure of stretchable hybrid nanogenerator device consisted of two major parts: i) a top layer of stretchable ZnO NW array on ZnO NW-embedded PDMS which was sandwiched by double layers of Au/PDMS and ii) Al electrode. The details of the device fabrication were shown in Figure 5.1 (a). First, the stretchable ZnO NW array on ZnO NW-embedded PDMS was prepared as described in section 5.1. A 40 nm thickness of Au electrode was deposited on the stretchable ZnO NW array via reactive magnetron sputtering technique on both sides of device (i.e. PDMS and ZnO NW surface). It should be noted that the deposition was carried out in an argon gas pressure of 5.0×10^{-3} mbar and a power of 100 W. The thickness of Au film was controlled by using thickness monitor (INICON AQM-160) during deposition. Finally, such Au/ZnO NW-embedded PDMS/ZnO NW/Au layer was sandwiched by PDMS membrane with a thickness of 300 μm . The performance of nanogenerator was characterized in terms of the output voltage, current and power.

5.2.2 Performance of hybrid nanogenerator device base on stretchable ZnO NWs array

The total active area size of hybrid device is $1.5 \times 1.5 \text{ cm}^2$ as shown in Figure 5.1 (b). Figure 5.1 (c) exhibits the cross-sectional image of ZnO NWS with a length of $\sim 2 \mu\text{m}$ embedded into PDMS membrane, which was covered by Au/PDMS layer on the topside of ZnO NWs. Such piezoelectric layer based on ZnO NWs embedded into insulated PDMS membrane probably allows us to avoid non-uniform force distribution and reduce screening effect¹⁹. To understand working principle of the hybrid device, the electrical outputs of the hybrid device compared with a reference triboelectric (RT) device were measured. Noted that the difference between the hybrid device and the RT device is that there is no ZnO NWs grown on PDMS membrane inserted into RT device structure as shown in Figure 5.2.

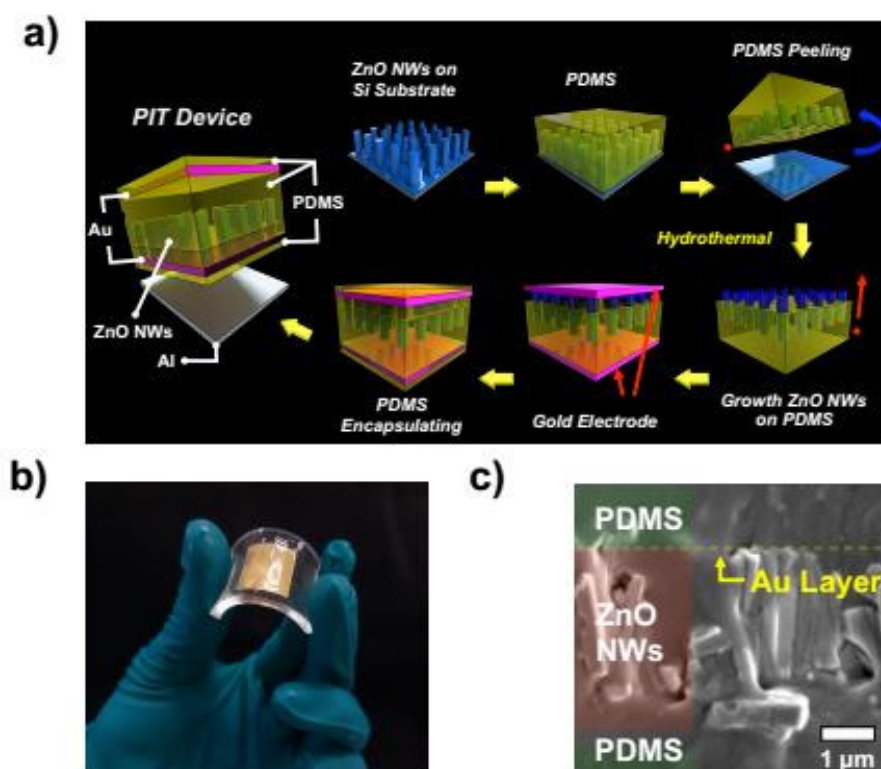


Figure 5.2 (a) a schematic diagram of hybrid device (b) the total active area size of hybrid device is $1.5 \times 1.5 \text{ cm}^2$ (c) the cross-sectional SEM image of ZnO NWs

Figure 5.2 (a) and 5.2 (d) show the cross-section of hybrid device and RT device, which were applied by vertical force of 0.8 N on the topside. Herein six sub-devices were separately measured in each major device such as Z1, Z2 and Z3 for the hybrid device and T1, T2 and T3 for the RT device. The structure of sub-device Z1, Z2 and Z3 comprise of Au/PDMS/ZnONWs/Au/PDMS-Al, Au/PDMS/ZnONWs/Au and Au/PDMS-Al whereas the structure of sub-device T1, T2 and T3 consist of Au/PDMS/Au/PDMS-Al, Au/PDMS/Au and Au/PDMS-Al, respectively. Figure 5.2 (b) and 5.2 (c) exhibit the open circuit voltage (V_{oc}) and short circuit current (I_{sc}) of sub-device Z1, Z2 and Z3 as a function of time. On the other hand, the V_{oc} and I_{sc} of sub-device T1, T2 and T3 at the different of time are shown in figure 5.2 (e) and 5.2 (f). Noted that the frequency of applied force is 5 Hz. It can be seen that the average value of V_{oc} peaks of Z1, Z2 and Z3 sub-device are 0.11 V, 0.21 V and 0.82 V whereas the average value of I_{sc} peaks of Z1, Z2 and Z3 sub-device are 12 nA, 10 nA and 45 nA. On the other side, the average value of V_{oc} peaks of T1, T2 and T3 sub-device are 0.11 V, 0 V and 0.42 V, while the the average value of I_{sc} peaks of T1, T2 and T3 sub-device are 8 nA, 0 nA and 15 nA. Attributed to the basic mechanism of each sub-device, the electrical output production of Z1, Z3, T1 and T3 should directly come from the induction of triboelectric charge between PDMS surface (negative polarity) and Al surface (positive polarity) based on triboelectric series^{36,37,44,45}. On the other hand, the electrical converting output of sub-device Z2 relies on piezoelectric effect based on ZnO NWs. The absence of ZnO NWs in sub-device T2 should be the cause of undetectable electrical output due to the absence of piezoelectric layer. Generally, it has been known that the fundamental triboelectric device is a conjugation of contact electrification and electrostatic induction, which inherently rely on capacitive behavior^{37,38,46,47}. Therefore, the capability of electrical converting output of our triboelectric devices should be regularly depended on the ability of charge transfer between two triboelectric material surfaces⁴⁴ and the electric field inside triboelectric materials (i.e. dielectric strength) that produce the electrostatic charge induction on the surface of electrode contacted with dielectric materials³⁸. The former factor strongly relates to a difference in their triboelectric polarity of selected materials^{37,39,48,49}, while the later factor correlates with the thickness of the triboelectric materials⁵⁰. Since the top plate of sub-device Z1 and T1 are comprised of multilayer of Au/PDMS/ZnONWs/Au/PDMS and Au/PDMS/Au/PDMS which are

thicker than that of sub-device Z1 and T1 (i.e. Au/PDMS), the lower in electrical output value of sub-device Z1 and T1 compared to sub-device Z3 and T3 should be from the thickness effect. In other word, the thicker device layer results in lower the electric field strength in PDMS, which reduces the electrostatic induction in device ⁵¹. In addition, our results demonstrate that the insertion of ZnO NWs embedded on PDMS membrane dose not significantly effect on electrical converting output of triboelectric in sub-device Z1, resulting that the average value of Voc and Isc peak of sub-device Z1 and T1 are close to each other. Here we question that why the Voc and Isc peak of sub-device Z3 are higher than that of sub-device T3 for 2 and 3 folds, even though the triboelectric charge of both devices are generated from same couple of materials surface and structure of device (Au/PDMS-Al). Since the only distinction between sub-device Z3 and sub-device T3 is that the top Au electrode of sub-device Z3 connected to ZnO NWs (sub-device Z2) whereas top Au electrode of sub-device T3 contacted with PDMS layer (sub-device T2), the enhancement of electrical converting output in sub-device Z3 might be caused by piezo-potential of ZnO NWs affected on the top Au electrode ^{44,52,53}. Noted that there are no any surface modifications of PDMS layer and Al electrode on both devices. To understand how piezoelectric effect of ZnO NWs can raise the electrical converting output in triboelectric device, we have collected the Voc output signal of tribelectric sub-device Z3 in single press-and-release compared to the Voc of piezoelectric sub-device Z2 and the Voc of tribelectric sub-device T3 as shown in figure 5.3.

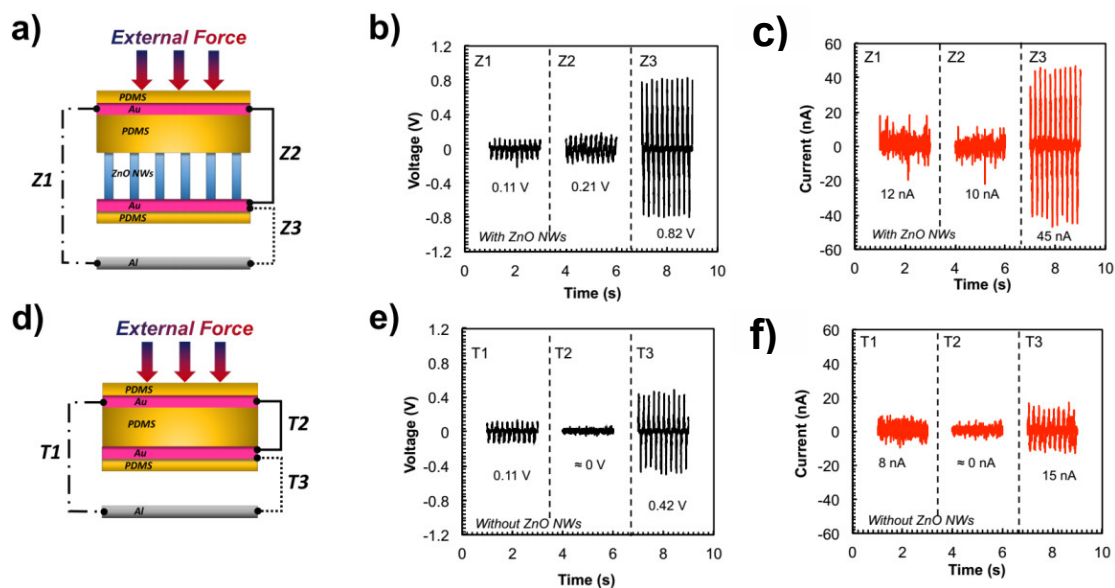


Figure 5.3 Show (a) the cross-section of hybrid device and (d) RT device, which were applied by vertical force of 0.8 N on the topside (b) the open circuit voltage (V_{oc}) and (c) short circuit current (I_{sc}) of sub-device Z1, Z2 and Z3 as a function of time (e) the V_{oc} and (f) I_{sc} of sub-device T1, T2 and T3 at the different of time.

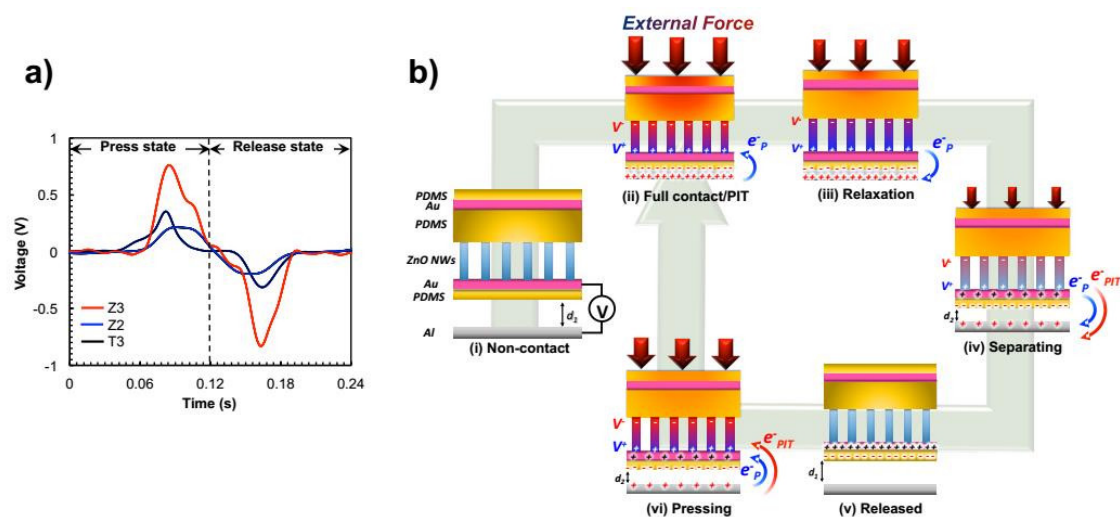


Figure 5.4 (a) Shows a schematic diagram of hybrid device (b) the total active area size of hybrid device is $1.5 \times 1.5 \text{ cm}^2$ (c) the cross-section image of ZnO NWs.

Figure 5.3 (a) shows the Voc characterization of triboelectric sub-device Z3 (red line), piezoelectric sub-device Z2 (blue line) and triboelectric sub-device T3 (black line) in single press-and-release as a function of time. The results exhibit that the Voc output signal of triboelectric sub-device Z3 comprises of a major peak and a shoulder at the pressing state whereas at the releasing state, a small pit and a major valley are observed. On the other hand, the Voc output signal of piezoelectric sub-device Z2 and triboelectric sub-device T3 compose of one major peak at the press state and a major valley at the release state. Interestingly, the occurrence period of the Voc peak and valley of piezoelectric sub-device Z2 cover the range of the occurrence period of the Voc of triboelectric sub-device Z3. On the other hand, the occurrence period of the Voc peak and valley of triboelectric sub-device T3 are consistent to the occurrence period of the major Voc peak at pressing stage and the major Voc valley at release state of triboelectric sub-device Z3. These imply that the triboelectric event of sub-device Z3 simultaneously appears with the period of piezoelectric event in sub-device Z2. Within the framework of triboelectric device based on metal-insulator contact, the surface charge on insulator surface ($\sigma_{\text{insulator}}$) strongly affect to the electrical converting output of triboelectric device. A larger value of $\sigma_{\text{insulator}}$ can induce a higher surface charge density on back contact electrode ($\sigma_{\text{electrode}}$), leading to an enhancement of the electrical converting output^{54,55}. Recently, J. Peng et al. reported that the increment of the transferred surface charge density on PDMS surface could be achieved through the positive charge CNCFS impregnated in PDMS, which boosted the potential difference with respect to the Fermi level of the contact metal⁴⁴. Therefore, the increase in Voc and Isc of sub-device Z3 might be attributed to the synergetic effect between piezoelectricity and triboelectricity that enhance the number of electron transfer and accumulation on the surface of PDMS. We further simulate the surface charge density generated by PIT and triboelectric based on the existing theoretical model of a conductor-to-dielectric contact-mode triboelectric. As a result, the enhancement of Voc of the structure including ZnO NWs is due to the piezo-potential that causes more charge transfer and accumulation on the electrode as shown in the red lines of Figure 5.4

Figure 5.3 (b) demonstrates the possible schematic diagram for operating mechanism of hybrid sub-device Z3 that refers from the measurement of force profile in a single press-and-release as a function of time as shown in figure 5.5. (i) At the initial state before contact of the two materials (i.e. PDMS and Al), neither triboelectric nor piezoelectric potential is occurred. (ii) When an external force applied on the top layer side (i.e. Au/PDMS/ZnONWs/Au/PDMS) to be in contact with Al surface, a physical contact between PDMS and Al electrode causes the charge transfer. Since the a characteristic energy level of PDMS is lower than the work function of Al, the electrons trends to flow from the filled Fermi level (E_F) of Al to surface of PDMS, resulting in the positive charge on Al surface ⁴⁴. At the same time, the tensile strength is occurred via the bending of PDMS layer in sub-device Z2, which produces the positive piezo-potential at the tip of ZnO NWs due to stretched event ^{20,34}. Such positive piezo-potential on Au electrode not only drives electrons to flow across external circuit in order to compensate the potential difference between Au electrode and Al electrode as shown in figure 5.6 but also simultaneously produces a net electric field along the direction from PDMS to Al electrode, resulting that more electrons transfer from Al to the surface of PDMS owing to larger difference with respect to the Fermi level of contacted metal ^{44,52}. (iii) Once the external force is released (PDMS still contacts with Al), the piezoelectric electrons (e_p) flow back to the Al electrode due to the reduction of piezo-potential. The small pit is then observed. (iv) During residual strain in ZnO NWs is releasing, the PDMS suddenly separates from Al surface. Accordingly, the triboelectric electrons begin to transfer to the Al electrode through the external circuit to neutralize the positive triboelectric charges. Since the amount of surface charges density on PDMS are generated from the synergetic effect between triboelectricity and piezoelectricity as called piezo-induced triboelectric (PIT), the total number of electrons (e_{pit}) flowed from Au electrode to Al electrode during electrostatic charge induction process is much higher than that of conventional tribelectric devices (sub-device T3). (v) The triboelectric electrons transfer from Au electrode to Al electrode until reaching an electrostatic equilibrium. On the other hand, the piezoelectric electrons (e_p) still flow to Al electrode until on longer piezo-potential. This is the first half of hybrid device cycle. (vi) When the hybrid device is compressed again, the electrostatic equilibrium in triboelectric device is broken, resulting that electron flow back from Al electrode to Au electrode. At the

same time, the positive piezo-potential abruptly occurs at the tip of ZnO NWs contacted with the topside of Au electrode of sub-device Z3. Such positive piezo-potential not only drives piezo-electron from Al electrode to Au electrode but also increases the built in potential of triboelectric device ⁵², resulting that the electrical converting output of sub-device Z3 is elevated. Although the electrostatic equilibrium in triboelectric device seem to be reached when the surface of PDMS and Al are contacted together (i.e. no longer tribo-electrons), the piezo potential persistently appears due to the softness of PDMS layer ^{52,56}. Consequently, the piezo-electron and the residual tribo-electron boosted up through piezo-potential are continually flowed from Au electrode to Al electrode (i.e. small shoulder is found). This is a second half of hybrid device cycle. To confirm the effect of positive piezo-potential on the topside of Au electrode that enriches the electrical converting output of sub-device Z3, here we have investigated the electrical converting output of sub-device Z3 which applied by the external force from different direction as a function of frequency as shown in figure 5.7.

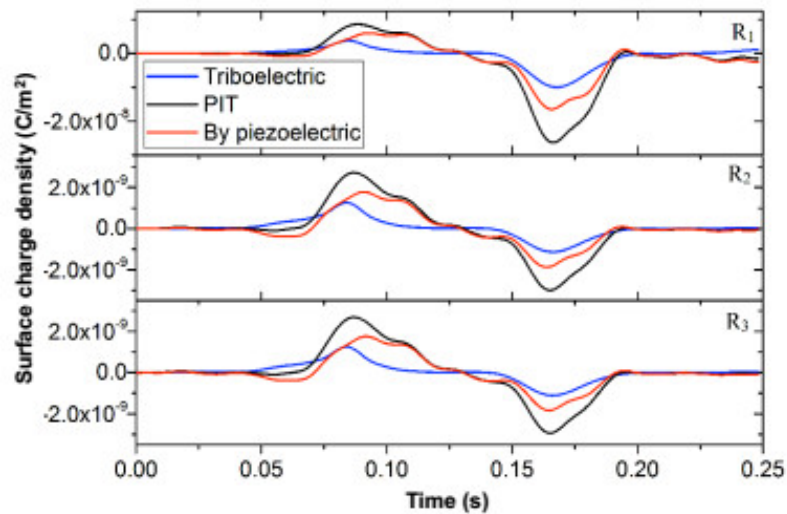


Figure 5.5 Calculated variation of surface charge density (σ) and time (t) at different load resistances of $R_1=10^{11}$, $R_2=10^{13}$, and $R_3=10^{15}$ Ω .

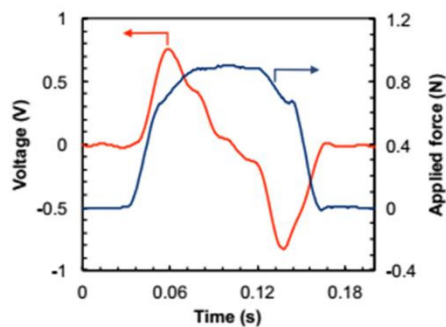


Figure 5.6 Force profile in a single press-and-release as a function of time

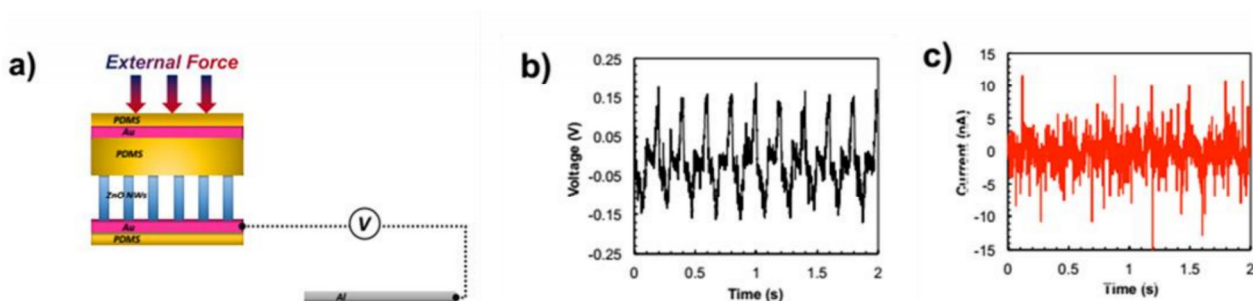


Figure 5.7 (a) The cross-section of hybrid device without Al (b) the V_{oc} and (c) I_{sc} value of sub-device Z3 applied by external force from topside

Figure 5.7 (a) and 5.7 (b) demonstrate the V_{oc} and I_{sc} value of sub-device Z3 applied by external force from topside (red line) and bottom side (blue line) at various force frequency. Noted that the black dash line in figure 5.7 (a) and 5.7 (b) are the V_{oc} and I_{sc} value of the reference conventional triboelectric device (T3). The external force is 0.8 N. The results show that the V_{oc} value of sub-device 3 compressed from the topside increases from 0.15 V to 0.83 V when the frequency was varied from 1 Hz to 5 Hz while the I_{sc} value increase from 14 nA to 45 nA. This indicates that the external electrons flow to reach equilibrium in a shorter time, which will lead to larger electrical converting output⁵⁷⁻⁵⁹. When the external force applied from the bottom side of sub-device 3, on the other hand, the V_{oc} values slightly increase from 0.06 to 0.11 V whereas the I_{sc} value slightly increase from 7 nA to 9 nA with

increasing the force frequency. Intriguingly, such Voc and Isc value obtained from the bottom side force are not only lower than that of the Voc and Isc value of the force applied from topside direction in sub-device 3 but also lower than that of the Voc and Isc value of the conventional triboelectric device (Voc = 0.06 to 0.45V and Isc = 8 nA to 14 nA), implying that the different direction of applied force compressed on sub-device Z3 strongly affect on the electrical converting output. Since the opposite applied force direction can be attributed to the opposite piezo-potential direction along c-axis of ZnO NWs⁶⁰, the piezo-potential on the top Au electrode compressed through the bottom side (Al electrode) should be the negative potential which will be produce a net electric field along the direction from Al to PDMS⁶⁰. Therefore, the net electric field created via negative potential might decrease the potential difference with respect to Fermi level of contacted metal (Al) and suppress electron to transfer to PDMS in electrification process, resulting that the tiny signal of electrical converting output could be observed. Conversely, the positive piezo-potential on the top Au electrode compressed through the topside could enhance the electrical converting output. Noted that the electrical converting output of conventional triboelectric sub-device T3 dose not change, even though it was applied by different force direction. In addition, we found that utilizing the stronger piezo-potential of Ag-doped ZnO NWs instead of the piezo-potential of ZnO NWs in sub-device Z3 allows us to produce the higher electrical converting output as shown in figure 5.8. Thus our results highlight that the enrichment of the electrical converting output of triboelectric device through boosting up the electron transfer and induced extra surface charge density could be achieved by utilizing piezo-potential of ZnO NWs.

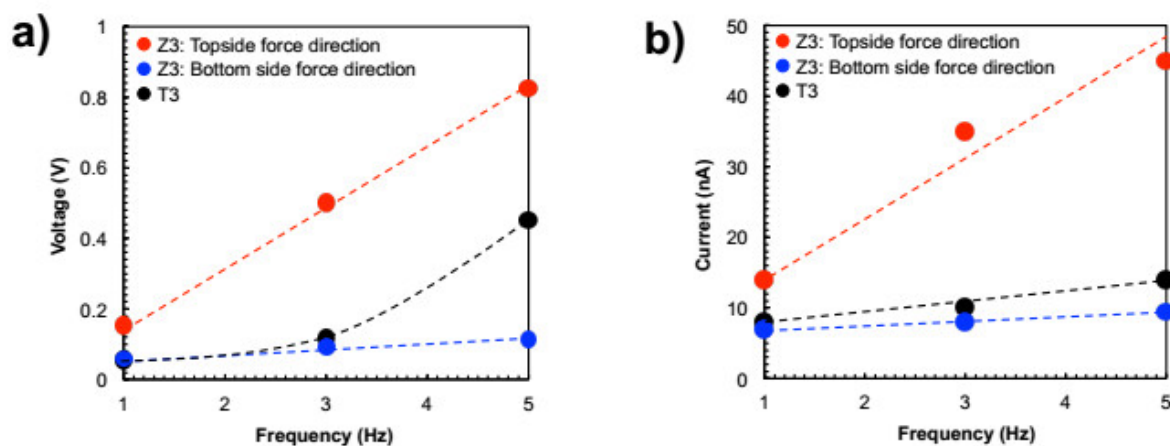


Figure 5.8 (a) Demonstrate the Voc and (b) Isc value of sub-device Z3 applied by external force from topside (red line) and bottom side (blue line) at various force frequency

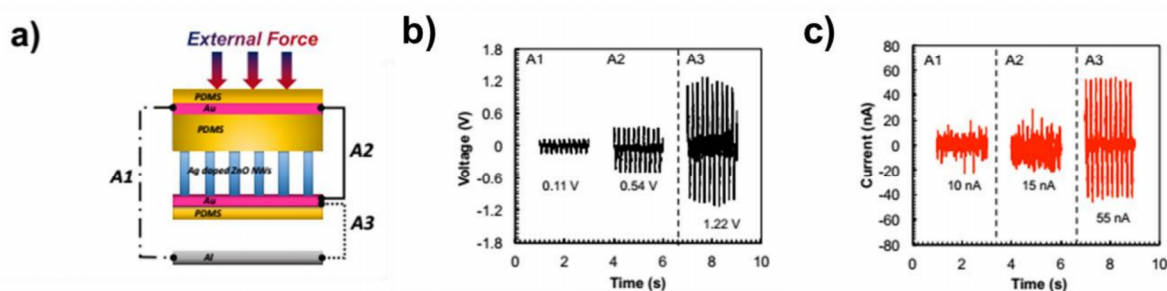


Figure 5.9 (a) The cross-section of hybrid device with Ag doped ZnO NWs (b) the Voc and (c) Isc value of sub-device Z3 applied by external force from topside

Figure 5.9 (a) and 5.9 (b) exhibits the output voltage and current at various resistances of sub-device Z3 and conventional triboelectric sub-device T3. Noted that the external applied force and frequency are 0.8 N and 5 Hz. As the load resistance increases, the amplitude of output current peaks is observed to drop whereas the voltage output peaks increase and then seems to be saturate. The peak power densities corresponding to load resistances are calculated as the product of corresponding current and voltage⁴⁰ as shown in figure 5.9 (b) and 5.9 (d). It can see that the maximum power of sub-device Z3 is 8.74 nW/cm²

at the matched load of 22Ω . On the other hand, the maximum power of sub-device T3 is 0.86 nW/cm^2 at the matched load of 7Ω . This indicates that the hybrid sub-device Z3 could generate output power density higher than that of conventional triboelectric sub-device T3 10 folds.

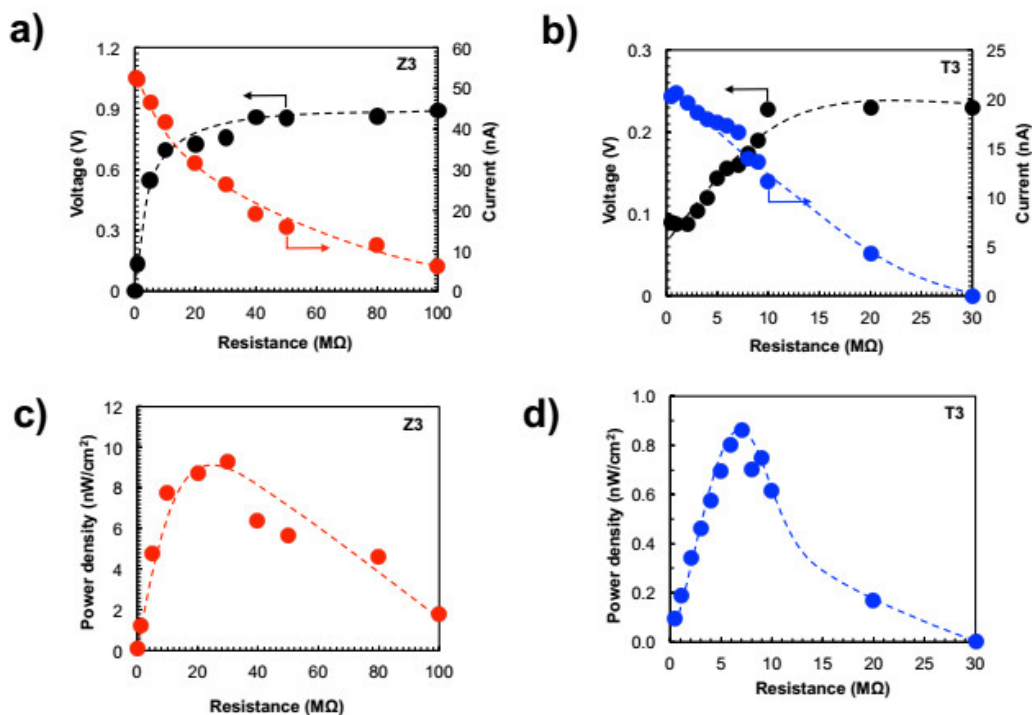


Figure 5.10 (a) The output voltage and (b) current at various resistances of sub-device Z3 and conventional triboelectric sub-device T3 (c) the peak power densities corresponding to load resistances are calculated as the product of corresponding current and voltage of sub-device Z3 and (d) triboelectric sub-device T3.

Finally, we have directly illuminated LEDs in the series connected to our PIT device as shown in figure 5.10 (a) and 5.10 (b). In this experiment, we utilized the finger force of 8.5 N calibrated via force sensor (Inter link force tester, No.402) to apply on our device. The results show that the output power from device Z3 without any external load resistor could light up to 100 LEDs. The details of rectified V_{oc} and current density output value during applied finger force are shown in figure 5.10 (c) and 5.10 (d). The average value of rectified V_{oc} peak is $\sim 60 \text{ V}$ while the average value of I_{sc} peak is $\sim 2.0 \mu\text{A/cm}^2$. The maximum power is $50 \mu\text{W/cm}^2$.

Thus, our results highlight that the rapid enhancement of triboelectric output can be achieved by using the piezo-potential as called piezo-induced triboelectric device. This discovery might eventually lead to high efficient nanogenerators applicable for various self-power electronics such as wearable, and mobile devices.

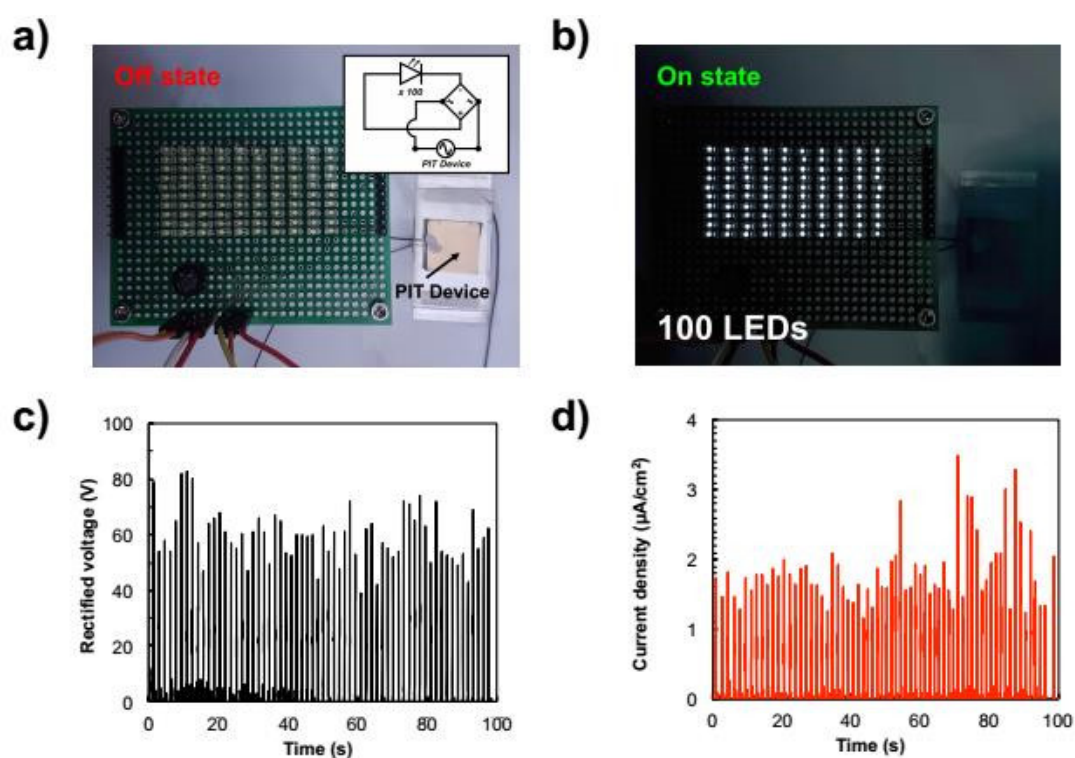


Figure 5.11 Show (a) 100 LEDs in the series connected (b) the output power from device Z3 without any external load resistor could light up to 100 LEDs (c) the V_{oc} and (d) current density output value during applied finger force.

5.3 Stretchable ZnO NW array for hybrid nanogenerators Volatile organic compound (VOC) sensor

5.3.1 Fabrication of stretchable ZnO NW array for VOC sensor

The fabricated stretchable ZnO NW array on ZnO NW-embedded PDMS was demonstrated as gas sensor. The structure of stretchable gas sensor device was consisted of the stretchable ZnO NW array on ZnO NW-embedded PDMS as sensing material, Au electrode with a gap of approximately 5 mm and a top PDMS as encapsulation. The details of the device fabrication were shown in figure 6.1. First, ZnO NWs with the length of 2 μm were prepared by same method as in section 3.1 on $1.5 \times 2 \text{ cm}^2$ of polyethylene terephthalate (PET) substrate. The stretchable ZnO NW array on ZnO NW-embedded PDMS was prepared as the same method described in section 5.1. A 200 nm thickness of Au electrode was deposited via reactive magnetron sputtering technique with a gap of 5 mm on left and right sides of the device. The performance of the sensor was characterized in term of resistance change upon VOC vapor exposure.

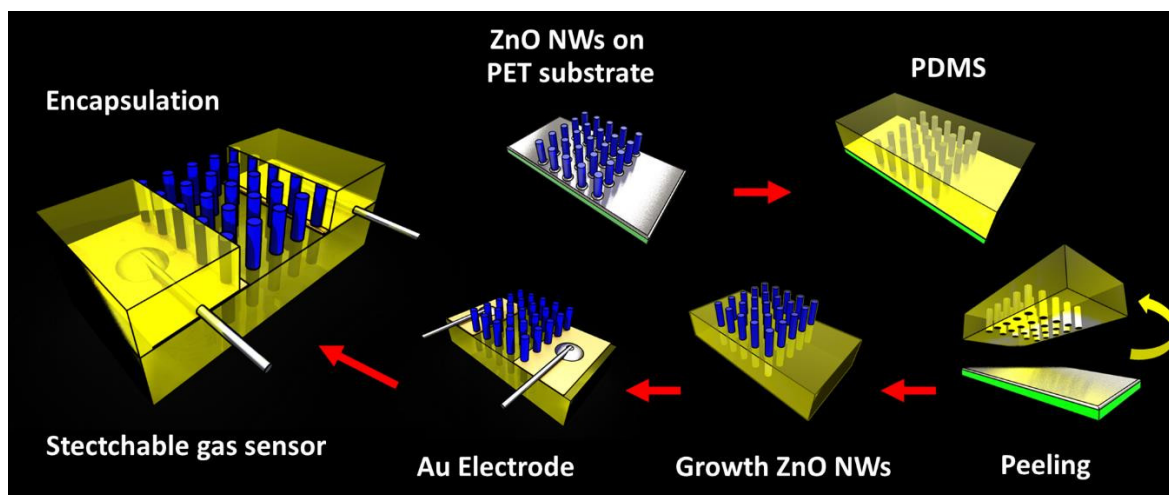


Figure 5.12 Schematic view of Stretchable gas sensor device

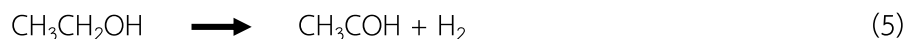
5.3.2 Performance of VOC sensor base on stretchable ZnO NWs array

Figure 5.12 show the resistivity-time curves of ZnO NWs when UV light is on and off. We could see that the UV light can enhance ZnO NWs conductivity, and ZnO NWs shows good reversibility. The dynamic response was stable and reproducible.

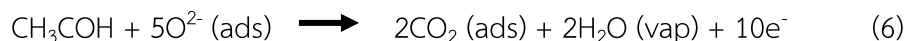
Zinc oxide sensors are known to be sensitive of various organic vapors. Hence some selectivity measurements have also been performed and presented in Figure. 5.13. These sensors were tested in presence of ethanol, acetone and methanol. It is found that responses of ethanol, acetone and toluene are 0.096, 0.028 and 0.025, respectively. The response of acetone and toluene are around 3.43 times lower than ethanol. Here the ZnO sensors are selective towards ethanol. For sensing mechanism of ZnO NWs. When the semiconductor metal oxides are exposed to air, the oxygen molecules are adsorbed on the surface of the materials. At room temperature the oxygen molecules are physisorbed. As the ZnO NWs under UV light, oxygen molecules are dissociated to oxygen ion. Different oxygen species (O_2 , O , O^{2-}) are created.



These oxygen species will take electrons from the conduction band of the ZnO and chemisorbed on the surface. This creates an electron depletion layer on the surface of the material which increases the resistance of the sensing. Ethanol interaction with metal oxide is complicated. Depending on the acid, base property of metal oxide ethanol will be decomposed to an intermediate state either to ethylene (dehydration) or acetaldehyde (dehydrogenation). As ZnO is a basic oxide, ethanol will be converted to acetaldehyde by the following equation.



Acetaldehyde will be further oxidised by interacting with the chemisorbed oxygen species. O_2 species will mainly interact with ethanol by the following equation



It can be seen from the above equation that the electrons will be freed due to the reaction with ethanol and returned back to the conduction band of ZnO NWs. Hence, the resistance of the ZnO NWs will decrease in presence of ethanol.

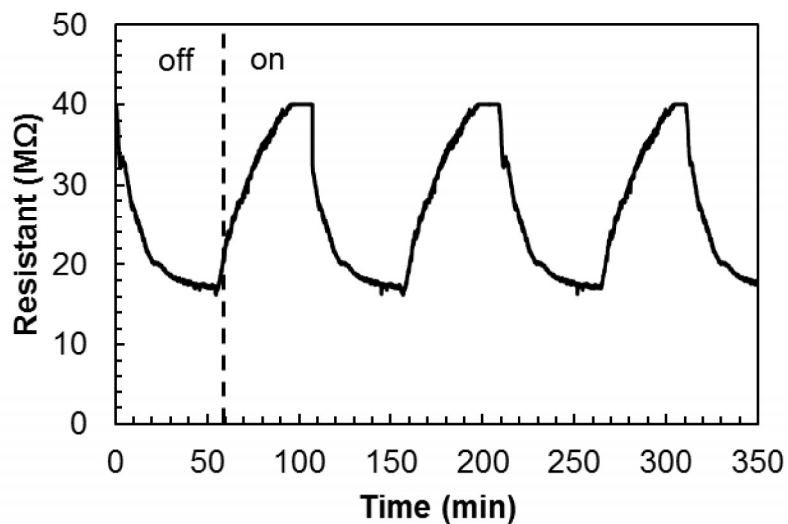


Figure 5.13. The resistivity-time curves of ZnO NWs when UV light is on and off.

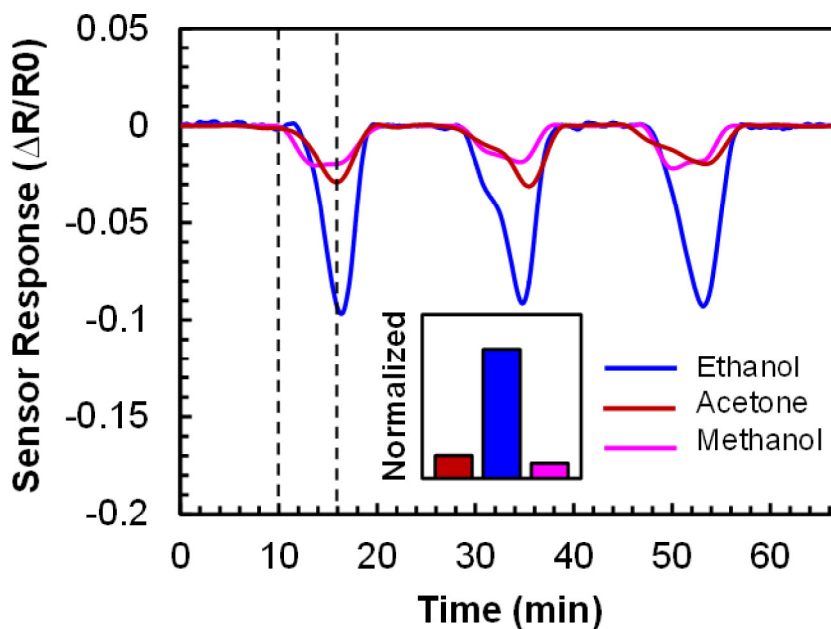


Figure 5.14 Selectivity measurements of ZnO NWs for Ethanol, Acetone and Methanol.

Figure 5.14 show the ethanol sensing response of stretchable gas sensor while bending with different angle 0° , 30° and -30° , respectively. We found that the sensor response slightly reduced from 0.096, 0.082 and 0.064, respectively. This result indicated that stretchable gas sensor can sensing ethanol gas while bending.

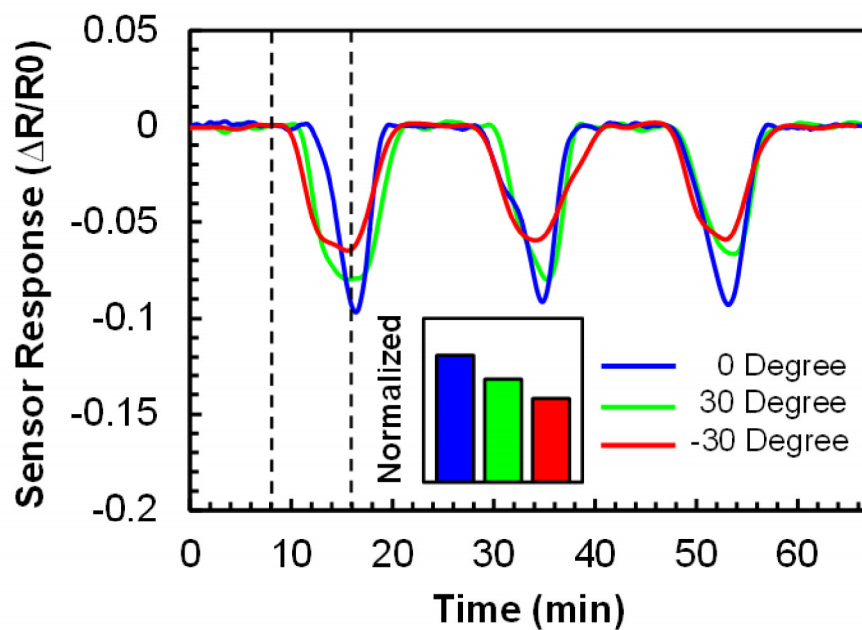


Figure 5.15 Ethanol sensing response of stretchable gas sensor while bending with different angle from -30° to 30° .

REFERENCES

- 1 M. Law, L. E. Greene, J. C. Johnson, R. Saykally and P. Yang, *Nat. Mater.*, 2005, **4**, 455–459.
- 2 C. Pan, L. Dong, G. Zhu, S. Niu, R. Yu, Q. Yang, Y. Liu and Z. L. Wang, *Nat. Photonics*, 2013, **7**, 752–758.
- 3 Q. Yang, Y. Liu, C. Pan, J. Chen, X. Wen and Z. L. Wang, *Nano Lett.*, 2013, **13**, 607–613.
- 4 L. Guo, H. Zhang, D. Zhao, B. Li, Z. Zhang, M. Jiang and D. Shen, *Sensors Actuators, B Chem.*, 2012, **166–167**, 12–16.
- 5 R. Hinchet, S. Lee, G. Ardila, L. Montès, M. Mouis and Z. L. Wang, *Adv. Funct. Mater.*, 2014, **24**, 971–977.
- 6 R. Kumar, O. Al-Dossary, G. Kumar and A. Umar, *Nano-Micro Lett.*, 2015, **7**, 97–120.
- 7 L. E. Greene, M. Law, J. Goldberger, F. Kim, J. C. Johnson, Y. Zhang, R. J. Saykally and P. Yang, *Angew. Chemie - Int. Ed.*, 2003, **42**, 3031–3034.
- 8 S. Xu, Y. Wei, M. Kirkham, J. Liu, W. Mai, D. Davidovic, R. L. Snyder and L. W. Zhong, *J. Am. Chem. Soc.*, 2008, **130**, 14958–14959.
- 9 C. P. Grigoropoulos and H. J. Sung, *Nano*, 2010, 666–671.
- 10 Baruah and J. Dutta, *Sci. Technol. Adv. Mater.*, 2009, **10**, 13001.
- 11 J. Joo, B. Y. Chow, M. Prakash, E. S. Boyden and J. M. Jacobson, *Nat. Mater.*, 2011, **10**, 596–601.
- 12 L. E. Greene, M. Law, D. H. Tan, M. Montano, J. Goldberger, G. Somorjai and P. Yang, *Nano Lett.*, 2005, **5**, 1231–1236.

- 13 P. Kasamechonchung, M. Horprathum, K. Boonpavanitchakul, N. Supaka, P. Prompinit, W. Kangwansupamonkon, A. Somboonkaew, J. Wetcharungsri, S. Pratontep, S. Porntheeraphat and A. Klamchuen, *Phys. Status Solidi*, 2015, **212**, 394–400.
- 14 A. Gulino and I. Fragala, *Chem. Mater.*, 2002, **14**, 116–121.
- 15 H.-J. Egelhaaf and D. Oelkrug, *J. Cryst. Growth*, 1996, **161**, 190–194.
- 16 S. B. Zhang, S.-H. Wei and A. Zunger, *Phys. Rev. B*, 2001, **63**, 75205-75209.
- 17 Y. Yan, M. M. Al-Jassim and S. H. Wei, *Appl. Phys. Lett.*, 2006, **89**, 181912-181917.
- 18 Y. Li, X. Zhao and W. Fan, *J. Phys. Chem. C*, 2011, **115**, 3552–3557.
- 19 D. Yang, Y. Qiu, Q. Jiang, Z. Guo, W. Song, J. Xu, Y. Zong, Q. Feng and X. Sun, *Appl. Phys. Lett.*, 2016, **3**, 41306-41310.
- 20 Z. L. Wang and J. Song, *Science (80-.)*, 2006, **312**, 242–246.
- 21 J. Zhou, N. Xu and Z. L. Wang, *Adv. Mater.*, 2006, **18**, 2432–2435.
- 22 C. F. Klingshirn, *ChemPhysChem*, 2007, **8**, 782–803.
- 23 A. Hernández Battez, R. González, J. L. Viesca, J. E. Fernández, J. M. Díaz Fernández, A. Machado, R. Chou and J. Riba, *Wear*, 2008, **265**, 422–428.
- 24 Z. L. Wang, *Mater. Today*, 2004, **7**, 26–33.
- 25 Y. Zhang, M. K. Ram, E. K. Stefanakos and D. Y. Goswami, *J. Nanomater.*, 2012, **2012**, 624520-624542
- 26 M. Sinha, R. Mahapatra, B. Mondal, T. Maruyama and R. Ghosh, *J. Phys. Chem. C*, 2016, **120**, 3019–3025.
- 27 K. H. Kim, K. Y. Lee, J. S. Seo, B. Kumar and S. W. Kim, *Small*, 2011, **7**, 2577–2580.
- 28 J. Chang, Y. Kuga, I. Mora-Seró, T. Toyoda, Y. Ogomi, S. Hayase, J. Bisquert and Q.

- Shen, *Nanoscale*, 2015, **7**, 5446–5456.
- 29 P. D. Yang, H. Q. Yan, S. Mao, R. Russo, J. Johnson, R. Saykally, N. Morris, J. Pham, R. R. He and H. J. Choi, *Adv. Funct. Mater.*, 2002, **12**, 323–331.
- 30 J. Steele, R. Lewis, J. Horvat, *Sci. Report.*, 2016, **6**, 28860- 28866
- 31 W. Lan, X. Peng, X. Liu, Z. He and Y. Wang, *Front. Mater. Sci. China*, 2007, **1**, 88–91.
- 32 L. Znaidi, *Mater. Sci. Eng. B Solid-State Mater. Adv. Technol.*, 2010, **174**, 18–30.
- 33 Y. Zi and Z. L. Wang, *APL Mat.*, 2017, **5**, 74103-74122
- 34 Z. L. Wang, and J. Song, *Science*, 2016, **312**. 242-246.
- 35 I. Journal, 2016, 1274–1291.
- 36 S. Wang, L. Lin and Z. L. Wang, *Nano Lett.*, 2012, **12**, 6339–6346.
- 37 Z. L. Wang, *R. Soc. Chem.*, 2014, **35**, 1–12.
- 38 S. Niu and Z. L. Wang, *Nano Energy*, 2014, **14**, 161–192.
- 39 Z. L. Wang, L. Lin, J. Chen, S. Niu and Y. Zi, *Springer*, 2016, **1**, 1865-3529.
- 40 Z. L. Wang, J. Chen and L. Lin, *Energy Environ. Sci.*, 2015, **8**, 2250–2282.
- 41 M. Que, R. Zhou, X. Wang, Z. Yuan, G. Hu and C. Pan, *J. Phys. Condens. Matter*, 2016, **28**, 433001.
- 42 A. I. Ayesh, *J. Nanomater.*, 2016, **2016**, 2359-2375.
- 43 C. Wang, L. Yin, L. Zhang, D. Xiang and R. Gao, *Sensors*, 2010, **10**, 2088–2106.
- 44 J. Peng, H. Zhang, Q. Zheng, C. M. Clemons, R. C. Sabo, S. Gong, Z. Ma and L.-S. Turng, *Nanoscale*, 2017, **9**, 1428–1433.
- 45 K. Y. Lee, J. Chun, J. H. Lee, K. N. Kim, N. R. Kang, J. Y. Kim, M. H. Kim, K. S. Shin, M. K. Gupta, J. M. Baik and S. W. Kim, *Adv. Mater.*, 2014, **26**, 5037–5042.

- 46 V. D. C. Generators, R. O. Donnell, N. Schofield, A. C. Smith, S. Member and J. Cullen, 2009, **45**, 1778–1784.
- 47 S. Niu, Y. Liu, S. Wang, L. Lin, Y. S. Zhou, Y. Hu and Z. L. Wang, *Adv. Mater.*, 2013, **25**, 6184–6193.
- 48 A. F. Diaz and R. M. Felix-Navarro, *J. Electrostat.*, 2004, **62**, 277–290.
- 49 D. K. Davies, *J. Phys. D. Appl. Phys.*, 1969, **2**, 1533-1542.
- 50 S. Niu, Y. S. Zhou, S. Wang, Y. Liu, L. Lin, Y. Bando and Z. L. Wang, *Nano Energy*, 2014, **8**, 150–156.
- 51 X. Yue, Y. Xi, C. Hu, X. He, S. Dai, L. Cheng and G. Wang, *RSC Adv.*, 2015, **5**, 32566–32571.
- 52 G. Suo, Y. Yu, Z. Zhang, S. Wang, P. Zhao, J. Li and X. Wang, *ACS Appl. Mater. Interfaces*, 2016, **8**, 34335–34341.
- 53 K. Jenkins, V. Nguyen, R. Zhu and R. Yang, *Sensors (Switzerland)*, 2015, **15**, 22914–22940.
- 54 Y. S. Zhou, S. Wang, Y. Yang, G. Zhu, S. Niu, Z. H. Lin, Y. Liu and Z. L. Wang, *Nano Lett.*, 2014, **14**, 1567–1572.
- 55 P. Bai, G. Zhu, Y. S. Zhou, S. Wang, J. Ma, G. Zhang and Z. L. Wang, *Nano Res.*, 2014, **7**, 990–997.
- 56 W.-S. Jung, M.-G. Kang, H. G. Moon, S.-H. Baek, S.-J. Yoon, Z.-L. Wang, S.-W. Kim and C.-Y. Kang, *Sci. Rep.*, 2015, **5**, 9309-9315.
- 57 J. Chun, B. U. Ye, J. W. Lee, D. Choi, C.-Y. Kang, S.-W. Kim, Z. L. Wang and J. M. Baik, *Nat. Commun.*, 2016, **7**, 12985-12991.

- 58 X. S. Zhang, M. Di Han, R. X. Wang, F. Y. Zhu, Z. H. Li, W. Wang and H. X. Zhang, *Nano Lett.*, 2013, **13**, 1168–1172.
- 59 X. Wang, B. Yang, J. Liu, Y. Zhu, C. Yang and Q. He, *Sci. Rep.*, 2016, **6**, 36409-36417.
- 60 Z. Gao, J. Zhou, Y. Gu, P. Fei, Y. Hao, G. Bao and Z. L. Wang, *J. Appl. Phys.*, 2009, **105**, 1–7.

AUTHOR BIOGRAPHY

Name-Surname Chaivanut Jirayupat

Date of Birth May 18, 1993

Present Address 48/32 Soi Ramkumheang 102, Ramkumheang Rd., Saphan-sung,
Saphan-sung, Bangkok, Thailand 10240

Education

2011-2015 Bachelor of Engineering (Nanomaterial Engineering)
King Mongkut's Institute of Technology Ladkrabang

Recent/relevant publication:

- (1) [Chaivanut Jirayupat](#), Winadda Wongwiriyan, Panita Kasamechonchung, Tuksadon Wuttikhun, Kittipong Tantisantisom, Yossawat Rayanasukha, Thanakorn Jiemsakul, Chookiat Tansarawiput, Monrudee Liangruksa, Paisan Khanchaitit, Mati Horprathum, Supanit Porntheeraphat and Annop Klamchuen
“Piezoelectric Induced Triboelectric (PIT) Hybrid Nanogenerator Based on ZnO Nanowires Layer Decorated on Au/PDMS-Al Structure for Enhanced Triboelectric Performance”
ACS Applied Materials & Interfaces, 2018, **10** (7), 6433–6440

- (2) Chaiyanut Jirayupat, Chanoknan Rattanabut, Winadda Wongwiriyan, Annop Klamchuen

“ZincOxide Microrod Array on Flexible Substrate via Two-Step Seed-Assisted Hydrothermal Growth and its Application as Gas Sensor”

The 35th MST International Conference, Chiang Mai, Proceeding, 2018.

- (3) Chaiyanut Jirayupat, Winadda Wongwiriyan, Panita Kasamechonchung, Tuksadon Wuttikhun, Annop Klamchuen

“Synthesis and Characterization of Ag-doped ZnO Nanowires via Seed assisted Hydrothermal Growth”

The 35th MST International Conference, Chiang Mai, Proceeding, 2018.

Honours and award

1. The B.Eng. scholarship: Young Scientist and Technologist Programme (YSTP).
2014-2015
2. The M.Sc. scholarship: Thailand Graduate Institute of Science and Technology (TGIST), 2015-2017
3. Poster award : International Conference on Science and Technology of Emerging Material 2016 under entitle of “Optical and Electrical Properties of Hydrothermal Growth Ag-doped Zinc Oxide Nanowires”